Surface kinetics of $BaGd_{1-x}La_xCo_2O_{6-\delta}$ for use as an anode material in proton ceramic electrolyser cells

Tord Svee

M. Sc Thesis

Group for Electrochemistry,
Department of Chemistry,
Faculty of Mathematics and Natural Sciences

University of Oslo

16 August 2021

Preface

I started my journey with the Electrochemistry research group (ELCHEM) back in 2019 as a bachelor student, working on one of the same compositions used in this thesis. The group alongside the whole community at SMN is incredibly welcoming, and it would not have been the same without Friday beers and seminars. Amongst them, I want to especially thank my supervisor Truls Norby and my co-supervisors Reidar Haugsrud, Ragnar Strandbakke, Vincent Thoréton and Daniel Clark for their patience and support. An extra thanks goes to all my colleagues at Coorstek Membrane Sciences for their inspiration and insight to what lies beyond studying a single electrode material.

I must also raise my glass for some of my fellow students in the group Håkon, Stian, Magnus, Erik and Kevin for their company and discussions, with a big toast to the latter for his harsh but excellent critique of my work. And to all the students and roommates I've had the joy of meeting through these five years, thank you for making it such a great time.

Towards the end I want to thank my friends and family in Bodø. I would never have made it this far without your love and support all the way from 1997 to this very day. And last but most importantly, a big thanks to my significant other, Stine, for your unconditional love and for getting me up on even the toughest days.

2020 turned out to be a different and more difficult year than anticipated with a global pandemic and all that it brings, but all of you have helped in your own ways. There are always too many people to name in a preface like this, though none of you are forgotten. Cheers!

University of Oslo, August 2021

Tord Svee

Summary

The main topic of this thesis is the surface kinetics of $BaGd_xLa_{1-x}Co_2O_{6-\delta}$ (BGLC), a mixed ionic electronic conducting double perovskite, with operation temperatures between 400-700 °C that shows potential for use as an anode in Proton Conducting Ceramic Electrolysers (PCEC). While showing promise the material is still limited by its surface reactions, notably adsorption and dissociation.

To test the variation in surface kinetics with the ratio of lanthanides on the A'-site, five compositions with differing lanthanide content was synthesised with a sol-gel synthesis path: BGLC19 ($BaGd_{0.1}La_{0.9}Co_2O_{6-\delta}$), BGLC37 ($BaGd_{0.3}La_{0.7}Co_2O_{6-\delta}$), BGLC55 ($BaGd_{0.5}La_{0.5}Co_2O_{6-\delta}$), BGLC73 ($BaGd_{0.7}La_{0.3}Co_2O_{6-\delta}$) and BGLC91 ($BaGd_{0.9}La_{0.1}Co_2O_{6-\delta}$). Acceptable phase purity was determined through X-ray diffractometry (XRD), the batches sieved into four different grain size ranges, with diameters of 63-45 µm being used for all later experiments. Scanning electron microscopy (SEM) and Brunauer-Emmett-Teller (BET) analysis were applied to examine the morphology and determine the specific surface area of the samples.

Pulse isotope exchange (PIE) and gas phase analysis (GPA) were used to examine the surface kinetics of the samples. The PIE data also allows us to extract the adsorption and incorporation energy of gas species from the total activation energy. Comparative measurements in 21% oxygen at 400 °C for BGLC19 with GPA and PIE resulted in surface exchange coefficients for oxygen of 6.8×10^{-5} mol $m^{-2}s^{-1}$ (PIE) and 1.3×10^{-5} mol $m^{-2}s^{-1}$ (GPA), with the difference being attributed to exchange rates in GPA being limited by gas diffusion in the chamber. An experiment was also performed with PIE on BGLC19 in 21% and 2% oxygen, resulting in surface exchange coefficients of 6.8×10^{-5} mol $m^{-2}s^{-1}$ (21%) and 1.2×10^{-4} mol $m^{-2}s^{-1}$ (2%) at 400 °C. The total activation energy E_0 for oxygen exchange was lower in 2% oxygen (0.84 eV in 2% vs 1.1 eV in 21%), but with a slightly higher adsorption energy E_{ads} (0.79 eV in 2% vs 0.62 eV in 21%).

Measurements were also performed with PIE in 2% oxygen across compositions, with BGLC55 showing the lowest incorporation energy E_{inc} for oxygen at 0.82 eV but with the highest E_0 (0.91 eV) and E_{ads} (0.92 eV) of the set. BGLC73 displayed the lowest values for total activation and adsorption energies at 0.62 eV (E_0) and 0.69 eV (E_{ads}). The highest surface exchange rates for oxygen were measured for BGLC19, BGLC73 and BGLC91 at over 1×10^{-4} mol $m^{-2}s^{-1}$, while the values for BGLC37 and BGLC55 were around 6×10^{-4} mol $m^{-2}s^{-1}$.

PIE experiments involving the exchange of water vapour were also performed on BGLC37 and BGLC91, with BGLC73 exchanging the most water up to 450 °C. With unclear data and very little to no D_2O measured by the mass spectrometer, these experiments remain inconclusive.

Abbreviations

BET	Brunauer-Emmett-Teller
BGC	$BaGdCo_2O_{6-\delta}$
BGLC	$BaGd_{1-x}La_xCo_2O_{6-\delta}$ (used when talking about all compositions)
BGLC(x)(y)	$BaGd_{0.x}La_{0.y}Co_2O_{6-\delta}$ (specific composition, e.g. BGLC37)
BLC	$BaLaCo_2O_{6-\delta}$
BZCY	Y-doped $BaZrO_3$-$BaCeO_3$ solid solution
DFT	Density Functional Theory
ELCHEM	Electrochemistry research group at UiO
GPA	Gas Phase Analysis
ICE	Internal Combustion Engine
MFC	Mass Flow Controller
MIEC	Mixed Ionic Electronic Conductor
MS	Mass Spectrometer
PCEC	Proton Ceramic Electrolyser Cell
PEME	Polymer Electrolyte Membrane Electrolyser
PIE	Pulse Isotope Exchange
P-MIEC	Proton-Mixed Ionic Electronic Conductor
SOEC	Solid Oxide Electrolyser Cell
TPB	Triple phase boundary
UiO	Universitetet i Oslo (University of Oslo)
XRD	X-ray Diffractometry

Contents

1 Introduction

1.1 Background and motivation

Facing a global climate crisis, several sectors around the world, ranging from transport to industry, need to look ahead to a fossil energy free future in order to cut carbon dioxide (CO_2) emissions. At the core of the problem lie the production of electricity and storage of energy. Renewable energy is readily available from multiple sources. Photovoltaic cells have seen a rapid decline in price in the last couple of decades and are seeing more widespread use [1]. Wind-based power is also seeing an increase, while hydroelectricity is already well established in countries with the appropriate geography and precipitation for it. The downside of these renewables is that their power production varies with weather and season. By storing excess power at the peak, this could be somewhat counteracted [2].

Energy storage is not just important for power grids reliant on renewables, but also in vehicles and portable devices. While battery powered vehicles dominated from the middle of the 1800's to the beginning of the 1900's, they were later outclassed by internal combustion engines (ICE's) as roads improved and the need for range increased [3]. One of the biggest advantages with an ICE is that it can be supplied with fuel, with a much higher energy density than batteries, from an external tank. As battery technology has improved both energy density and construction, this has allowed for smaller and more powerful batteries. This has led to a resurgence of the electric car and the introduction of more portable electric devices. But while modern battery technology can power a personal car for around 400-600 km, heavier vehicles like ships, planes and long haul trucks encounter the same problem with energy density and range as the personal car from the 1800's [2, 4].

Table 1 - Energy density of hydrogen, methane diesel and lithium-ion batteries compared [5-7].

Material	**Specific energy density (MJ/kg)**	**Volumetric energy density (MJ/L)**
Li-ion battery	~0.6	~1
Diesel	45.4	34.6
Methane	55.6	15.5
Hydrogen (700 bar)	143	5.6

If we are to phase out fossil fuels, hydrogen could be an alternative for storing and transporting larger amounts of energy. Hydrogen is, however, not an energy source, but an energy carrier, and must be synthesised. Today the most common way of doing this is through steam reformation of natural gas or oil, which still entails CO_2 emission [2]. If clean electricity is available, electrolysis is the alternative. The most common method of electrolysis of water to produce hydrogen gas is through alkaline cells. This method operates at low temperatures (80 °C), and involves high cell voltages of about 1.7-1.9 V, causing a significant loss of efficiency through heat development. Low temperature electrolysis is, however, a well-established technology, reaching conversion efficiencies up to 75% [8].

To increase this efficiency, it is possible to use solid, ceramic-based cells that can operate temperatures between 400-800 °C. As the electrolysis process is endothermic, an increase in temperature will decrease the demand for electric energy, while the heat and total energy demand increases (see Figure 1). If waste heat from nuclear power or industrial processes are available, an increased operating temperature would decrease the cost of producing hydrogen by lowering the need for electricity [9].

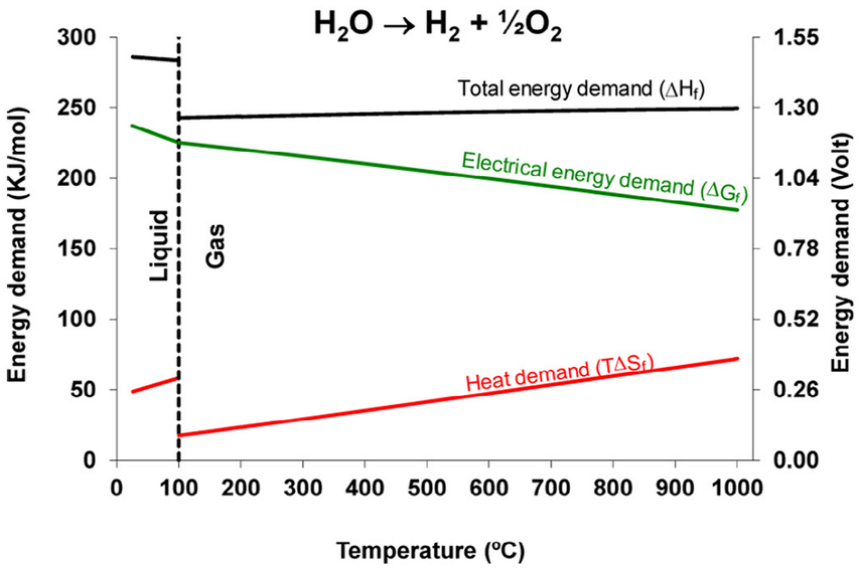

Figure 1 - Thermodynamics of water electrolysis at 1 bar H_20 [10].

Solid Oxide Electrolyser Cells (SOEC) and Proton Ceramic Electrolyser Cells (PCEC) are similar in this regard, where both use solid ceramic or metallic electrodes and electrolytes to operate at high temperatures. A SOEC passes water over the cathode, dissociated the atoms in the molecule, reduces the adsorbed hydrogen to hydrogen gas, and moves the oxygen as an ion through the membrane to be oxidised to gaseous form at the anode side. The resulting hydrogen gas is not completely dry in this case, requiring post-processing to dry the product. With a PCEC, the water is passed over the anode instead, with protons passing through the electrolyte, producing dry hydrogen, thus removing the need for drying the gas as seen in Figure 2 [9].

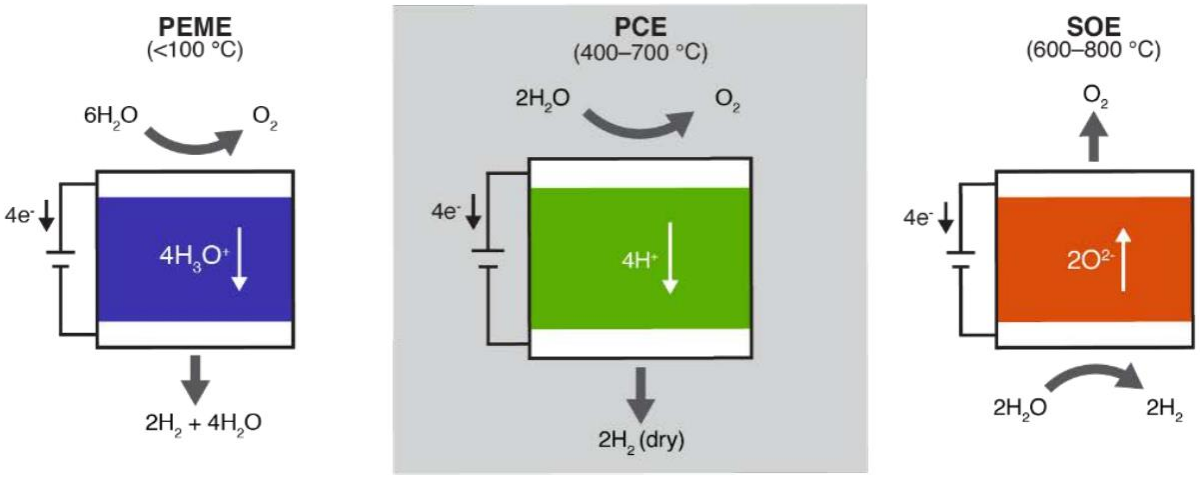

Figure 2 - Schematic comparison of Polymer Electrolyte Membrane Electrolysis (PEME), PCEC and SOEC.[11]

Some of the challenges for PCECs have been electronic leakage, and slow electrode kinetics, limiting the reaction rate. Recently is has been shown that a tubular cell, using $Ba_{1-x}Gd_{0.8}La_{0.2+x}O_{6-\delta}$ (BGLC) as an anode, can operate at 600 °C with a faradaic efficiency close to 100% at high steam pressures. As the rate limiting reaction for water splitting at existing BGLC based anodes is tied to both adsorption, dissociation and diffusion, there might still be room for improving the kinetics of the material. [11].

1.2 Project definition

The goal of this thesis is to learn how the surface exchange kinetics of BGLC behave with varying substitution of lanthanum and gadolinium, to determine which lanthanide content might be most suited for PCEC applications.

Five different compositions, ranging from $BaGd_{0.1}La_{0.9}Co_2O_{6-\delta}$ (BGLC19) to $BaGd_{0.9}La_{0.1}Co_2O_{6-\delta}$ (BGLC91) will be synthesized through a sol-gel synthesis path, and sieved to a narrower particle size distribution. Further characterization with scanning electron microscopy and Brunauer-Emmett-Teller analysis will be required to determine morphology and specific surface area. Each composition will then be evaluated with pulse isotope exchange and gas phase analysis to measure the isotope exchange rate of oxygen and water at chemical equilibrium.

2 Theoretical background

2.1 Defect chemistry

When a crystal deviates from its ideal structure either by the addition or removal of atoms at different sites, it is called a *defect*. Defects range from simple point defects like vacancies and substituted foreign atoms, to grain boundaries and clustered impurities. Intrinsic defects like Schottky or Frenkel defects are found in every crystal lattice above 0 K, as it is energetically favourable to increase disorder at non-zero temperatures. Defects are not always purely structural, as exchange of electron between species and bands also happens in materials.

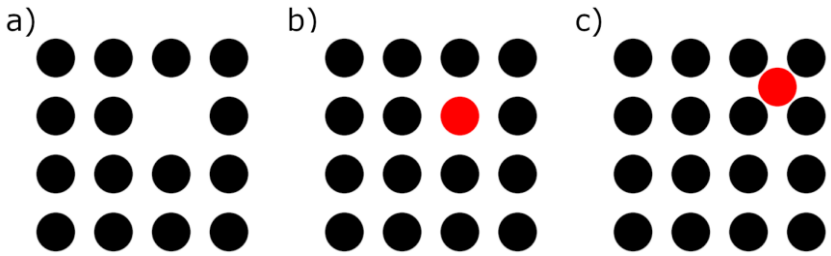

Figure 3 - Schematic of three common defects: a) vacancy b) substitutional foreign atom c) interstitial foreign atom.

Sometimes defects play a role in chemical reactions, such as oxygen vacancies being formed in an oxide upon heating. When defects are included in reaction equations, they are denoted with Kröger-Vink notation on the form A_S^C . A is either a chemical symbol, electron/hole or a vacancy (noted as *v*). *s* displays the crystal site it is located on, which can be either on an existing site or an interstitial site (noted as *i*). Lastly *c* is the effective charge of the defect, where • is positive, / negative and *x* neutral. For instance, oxygen in a BGLC lattice has an oxidation state of -2 and as long as oxygen is present here with that charge it can be written as O_O^x. If a vacancy is generated here, we will be lacking a charge, and it becomes effectively positively charged compared to the reference state, noted $v_O^{\bullet\bullet}$. When writing defect chemical reactions one must balance for both conservation of mass, charge and ratios of sites [12].

In BGLC we find both vacancies, electronic and substitutional defects. As the material is an oxide, some of the most important defect chemical reactions are the filling and generation of oxygen vacancies.

In oxidizing conditions, the following reaction takes place to fill vacancies:

$$\frac{1}{2}O_2(g) + v_O^{\bullet\bullet} = 2h^{\bullet} + O_O^x \quad (1)$$

Whereas the opposite will take place in reducing conditions:

$$O_O^x = v_O^{\bullet\bullet} + 2e' + \frac{1}{2}O_2(g) \quad (2)$$

In the case of BGLC, it contains cobalt which can take on three different oxidation states Co^{2+}, Co^{3+} and Co^{4+}. This allows the material to compensate its variable oxygen content through changing the oxidation states of cobalt. Since we have decided that the reference state of BGLC is the fully oxidized state, it means that the reference state of cobalt has an average charge of 3.5+. Thus Co^{2+} and Co^{3+} are effectively negatively charged, while Co^{4+} is positively charged [13].

Table 2 - Some possible defects in BGLC.

Defect	
O_O^x	Oxygen site
$v_O^{\bullet\bullet}$	Oxygen vacancy
$OH_O^{\bullet}$	Hydroxide
$Co_{Co}^{3/2\,\prime}$, $Co_{Co}^{1/2\,\prime}$ and $Co_{Co}^{1/2\,\bullet}$	Co^{2+}, Co^{3+} and Co^{4+}

As the intended use of the material is as a PCEC, we must also consider protonic defects. There are two ways of incorporating hydrogen into the lattice from water. The first is hydration, which makes use of oxygen vacancies.

$$H_2O(g) + O_O^x + v_O^{\bullet\bullet} = 2OH_O^{\bullet} \quad (3)$$

The second is hydrogenation, which balances the equation by generating free electrons and oxygen gas. As free electrons and electron holes are localized on cobalt in BGLC, we will change the oxidation state of two cobalt atoms instead of generating free electrons.

$$H_2O(g) + 2O_O^x + 2Co_{Co}^{1/2\bullet} = 2Co_{Co}^{1/2\prime} + 2OH_O^{\bullet} + \frac{1}{2}O_2(g) \quad (4)$$

Depending on stoichiometry, temperature and atmosphere both or one of these processes will be the mechanism for incorporating hydrogen in the sample from water vapor [14, 15].

If we write out the equilibrium constants for each, we can see how each process depends on the partial pressure of water and oxygen.

$$K_{hydration} = \frac{[OH_O^{\bullet}]^2}{p_{H_2O}[O_O^X][v_O^{\bullet\bullet}]} \quad (5)$$

$$K_{hydrogenation} = \frac{[OH_O^{\bullet}]^2[Co_{Co}^{1/2\prime}]^2 p_{O_2}^{1/2}}{[O_O^X]^2[Co_{Co}^{1/2\bullet}]^2 p_{H_2O}} \quad (6)$$

2.2 Surface reactions

The reactions for reduction, oxidation, incorporation, and exchange of gas all happen at the surface of BGLC. If the transport of species in the sample is quick enough, the surface kinetics will be the limiting factor. For protons to be incorporated in BGLC, water must first be adsorbed before going through a series of steps before protons are incorporated and oxygen desorbed.

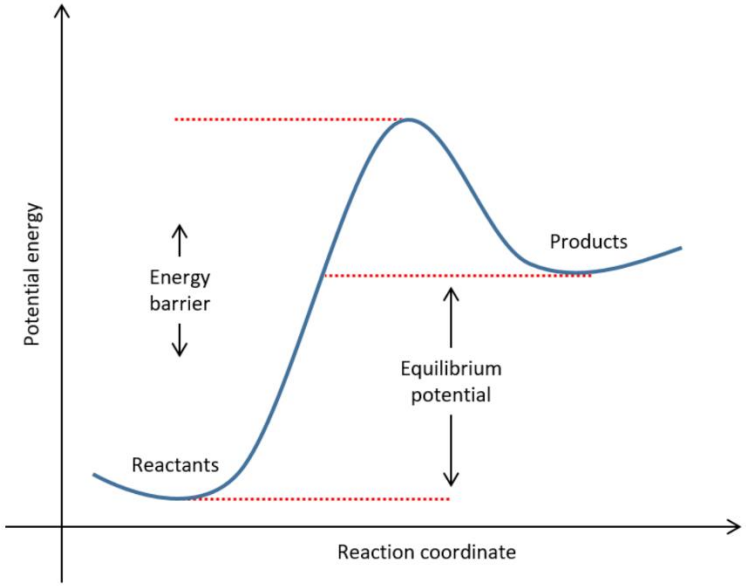

Figure 4 – Adapted illustration of activation energy in an endothermic process [16].

Each part of the reaction has an associated energy barrier that must be overcome. With increasing temperature, the average energy of particles becomes higher, and with it the probability of overcoming the energy barrier. This can be expressed in the Arrhenius equation (Equation 7), which relates the reaction rate *k* to temperature *T*, the universal gas constant *R*,

activation energy E_A and a pre-exponential factor A_0 which is a constant for each chemical reaction.

$$k = A_0 e^{-\left(\frac{E_A}{RT}\right)} \quad (7)$$

It can be difficult to know the exact reaction steps for a given reaction, but one example for proton conducting mixed ionic electronic conductors (P-MIEC) was suggested by Strandbakke et al. (see Table 3).

Table 3 - Examples of elementary reaction steps for a PCEC oxygen electrode reaction at a P-MIEC electrode [17].

Reaction step	**Elementary reaction**
1	$H_2O_{(g)} \rightleftharpoons H_2O_{(ads)}$
2	$H_2O_{(ads)} \rightleftharpoons O^{2-}_{(ads)} + 2H^+_{(surface,\ electrode)}$
3	$H^+_{(surface,\ electrode)} \rightleftharpoons H^+_{(interface,\ electrode)}$
4	$H^+_{(interface,\ electrode)} \rightleftharpoons 2H^+_{(electrolyte)}$
5	$O^{2-}_{(ads)} \rightleftharpoons O^-_{(ads)} + e^-$
6	$2O^-_{(ads)} \rightleftharpoons O_2{}^{2-}_{(ads)}$
7	$O_2{}^{2-}_{(ads)} \rightleftharpoons O_{2\ (ads)} + 2e^-$
8	$O_{2\ (ads)} \rightleftharpoons O_{2\ (g)}$

This process relies on both the electrode and electrolyte being proton conducting. With a non-ion conducting electrode the reaction is limited to the triple phase boundary (TPB) between gas phase, electrolyte and electrode, where the electrolyte can incorporate the ion and the electrode carry the electric current. By limiting the total available area, we are also limiting the total reaction rate. MIECs allow for much more use of the total surface area to be utilized by being able to conduct ions from the two-phase boundary between gas and electrode, to the electrolyte as illustrated in Figure 5 [18].

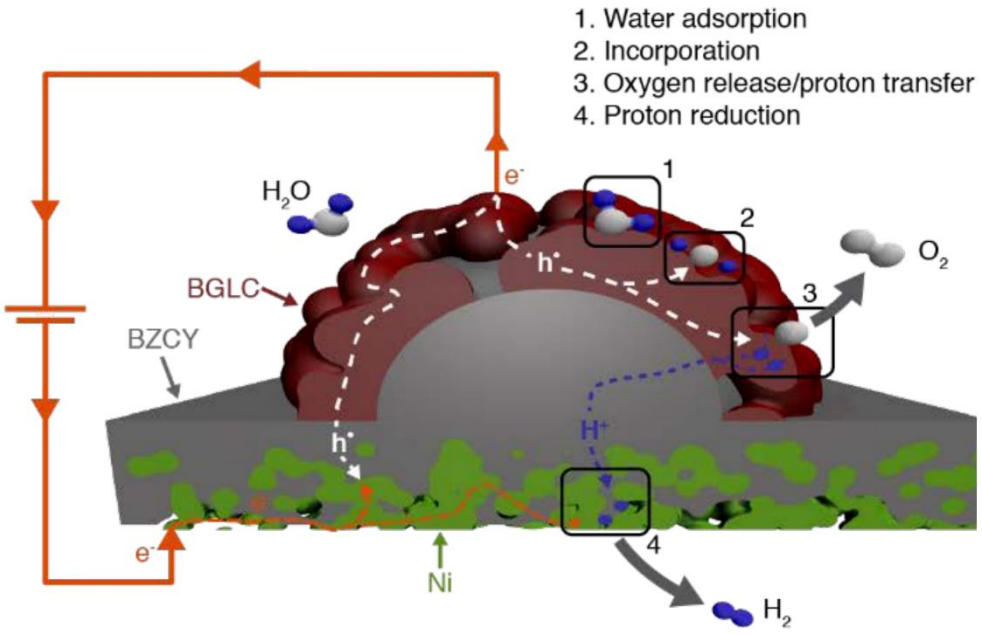

Figure 5 – Transport and mixed protonic and electronic conduction in a cell composed of BGLC deposited on BZCY as anode with nickel as cathode [11].

When gas species are adsorbed and dissociated on surfaces, they can heterogeneously exchange atoms with the sample, re-associate and desorb. One way of studying this process is by using different isotopes of the atoms in the annealing gas, like oxygen 18 (^{18}O) and deuterium (D). If we anneal a sample in $^{16}O_2$ and expose it to $^{18}O_2$, then the two isotopes might exchange atoms either in gas phase, on the surface, or between lattice and surface. Below are some of the reactions that might take place.

$$^{18}O_2(g) + {}^{16}O_O^X \rightleftharpoons {}^{18}O\,{}^{16}O\,(g) + {}^{18}O_O^X \quad (8)$$

$$^{18}O_2(g) + {}^{16}O_2(g) \rightleftharpoons 2\,{}^{18}O\,{}^{16}O\,(g) \quad (9)$$

$$D_2O\,(g) + OH_O^{\bullet} \rightleftharpoons DHO\,(g) + OD_O^{\bullet} \quad (10)$$

$$D_2O\,(g) + H_2O\,(g) \rightleftharpoons 2DHO\,(g) \quad (11)$$

By measuring the ratio of these species in gas phase over time, we can determine how quickly the process is happening, and its kinetics. This forms the basis of techniques such as Gas Phase Analysis (GPA) and Pulse Isotope Exchange (PIE).

2.3 Gas Phase Analysis

In GPA, tracer isotopes are utilized to measure the exchange rate of samples at chemical equilibrium. Since two isotopes behave the same chemically but have differing mass, we can use mass spectrometry to analyse the atmosphere as the sample exchanges gas with it. One way of doing this is by annealing a sample in $^{16}O_2$ at the desired temperature, quenching the sample and reaction chamber, pumping vacuum, switching to an $^{18}O_2$ atmosphere with the same partial pressure of oxygen, and returning it to temperature. Over time the sample will exchange atmospheric ^{18}O with ^{16}O bound in the sample to release $^{16}O_2$ and $^{18}O^{16}O$. By steadily leaking some of the atmosphere to a mass spectrometer, we can use the current of the masses corresponding to each isotope combination to determine the fraction of ^{18}O.

$$f_{18_O} = \frac{2I_{36} + I_{34}}{2(I_{36} + I_{34} + I_{32})} \tag{12}$$

Depending on the volume to surface ratio and the diffusion rates of the sample, the exchange rate will either be limited by diffusion or surface exchange or be in a mixed regime. In this thesis we mainly work with powders, and we can assume that the reaction is surface limited. With Boukamp's approach we can express the fraction of ^{18}O over time as.

$$f_{18_O}(t) = f_{18_O}(\infty) + \left(f_{18_O}(0) - f_{18_O}(\infty)\right)\exp\left(-Sc_0k\left(\frac{1}{N_g} + \frac{1}{N_s}\right)t\right) \tag{13}$$

Where S is the total surface area, c_0 the oxygen concentration in the oxide, k the surface exchange rate, N_g the number of atoms in the gas, N_s the number of atoms in the solid and t the time variable. This can then be rewritten to only have the exponential term on the right side of the equation.

$$\ln(\left[f_{18_O}(t) - f_{18_O}(\infty)\right]/[f_{18_O}(0) - f_{18_O}(\infty)]) = -Sc_0k\left(\frac{1}{N_g} + \frac{1}{N_s}\right)t \tag{14}$$

If we plot the left side of this equation for time, the slope will then be able to give us the surface exchange coefficient by multiplying k and c_0 [19].

2.4 Pulse Isotope Exchange

PIE is in several ways similar to GPA and relies on the same principles of equilibrium isotope exchange. However, instead of quenching, switching out the whole atmosphere of the reaction chamber and running the experiment for more than an hour, we send a small pulse of the corresponding isotope alongside a constant flow of the annealing gas before moving on to the next temperature step.

The powder sample used in PIE is loaded into a packed bed micro reactor, meaning that it is packed into a narrow tube of a heat resistant material like quartz with gas connections on each side, and the middle placed in a tubular furnace. The sample is then allowed to anneal and equilibrate at the chosen p_{O_2} and temperature, before the pulse is sent. The gas flowing out of the chamber can then be picked up by a mass spectrometer to be analysed as illustrated in Figure 6c.

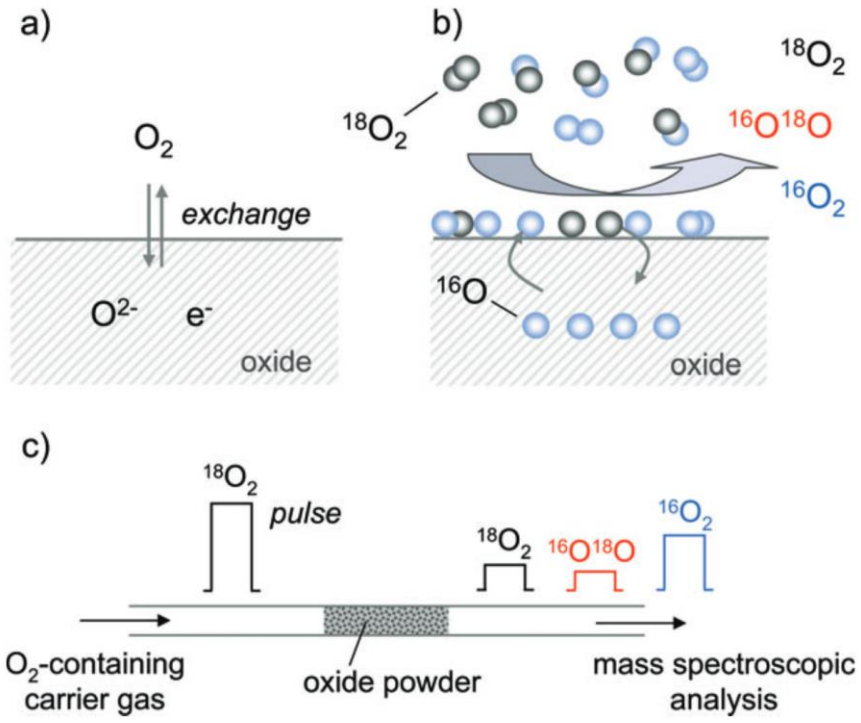

Figure 6 - a) Oxygen exchange between lattice and gas phase. b) Two step $^{18}O^{16}O$ formation mechanism from disassociated and adsorbed ^{18}O, and ^{16}O from the oxide. c) Schematic illustration of the pulse isotope technique [20].

The surface exchange rate of oxygen at equilibrium, $\Re_0$, is defined by the following equation:

$$n\frac{\partial f_g^{18}}{\partial t} = -\Re_0 S\left(f_g^{18} - f_O^{18}\right) \tag{15}$$

Where *n* is the total number of oxygen atoms in the gas phase, *S* the total available surface area, *t* time, and f_g^{18} and f_O^{18} the fraction of oxygen 18 in gas phase and the oxide. As the amount of ^{18}O in the sample is negligible, as very little of it is retained between experiments, we can assume that $f_O^{18} \approx 0$. For f_g^{18} we can express it with the two oxygen molecules containing ^{18}O, $f_g^{18} = f_g^{36} + 0.5 f_g^{34}$. Assuming ideal plug flow behaviour, the surface exchange rate can be expressed as:

$$\Re_0 = \frac{\mathrm{n}}{\tau_\mathrm{r} \mathrm{S}} \ln\left(\frac{\mathrm{f}_{\mathrm{g,i}}^{18}}{\mathrm{f}_{\mathrm{g,e}}^{18}}\right) \tag{16}$$

Where *i* and *e* denotes the fraction of the pulse at inlet and exit of the reactor. The inlet fraction is based on a reference measurement at room temperature where the sample does not exchange gas at a measurable rate. *S* is the total available surface area, which depends on the specific surface area and mass of the sample. Lastly τ_r is the average residence time of the gas in the reactor, which can be calculated from the flow rate and pulse volume [20, 21].

The surface exchange rate is however a parameter spanning two reaction steps, adsorption and incorporation, and can be broken down assuming only these two steps take place.

$$\Re_0 = \frac{\Re_\mathrm{a} \Re_\mathrm{i}}{\Re_\mathrm{a} + \Re_\mathrm{i}} = \mathrm{p} \Re_\mathrm{a} \tag{17}$$

Where $\Re_a$ is the rate of dissociative adsorption, $\Re_i$ the rate of incorporation of adsorbed atoms into the lattice, and *p* the probability of incorporation during the residence time on the surface. In order to find *p* we must derive it from the following equation:

$$\mathrm{f}_{\mathrm{g,e}}^{36} = \left(\frac{1-\mathrm{p}}{1-2\mathrm{p}} \mathrm{f}_{\mathrm{g,i}}^{18}\right)^2 \exp\left(-\frac{2\tau_\mathrm{r}}{\tau_\mathrm{u}}\right) + \left(\mathrm{f}_{\mathrm{g,i}}^{36} - \left(\frac{1-\mathrm{p}}{1-2\mathrm{p}} \mathrm{f}_{\mathrm{g,i}}^{18}\right)^2\right) \exp\left(-\frac{\tau_\mathrm{r}}{\mathrm{p}\tau_\mathrm{u}}\right) \tag{18}$$

Where $\tau_u = n/\Re_0 S$. As all other parameters in the equation are known, we can numerically fit a value for *p* to match the experimental data [22]. Then:

$$\Re_\mathrm{a} = \frac{\Re_0}{\mathrm{p}} \text{ and } \Re_\mathrm{i} = \frac{\Re_0}{1-\mathrm{p}} \tag{19}$$

If we know both $\Re_0$ and *p*, then calculating the rates for adsorption and incorporation is trivial.

3 Literature

3.1 Structural properties of BGLC

The structure of BGLC in most conditions is a layered double perovskite, with P4/mmm symmetry. This means that we have two perovskite type unit cells stacked on top of each other to generate two A and B sites in the structure, and can generally be described by the form (AA')(BB')$O_{6-\delta}$ (see Figure 7). The two A-sites contain barium and a lanthanide alternating along the c-axis, while cobalt is found on every B-site in an octahedral or square pyramidal configuration, depending on position and oxygen stoichiometry. If the barium content of the unit cell is equal to 1, it will prefer to be located on the A-site, while the lanthanides are situated on the A'-site. This way a structure with alternating layers of barium and lanthanides is formed [13]. It has also been shown that oxygen vacancies prefer to reside in the lanthanide layer [17].

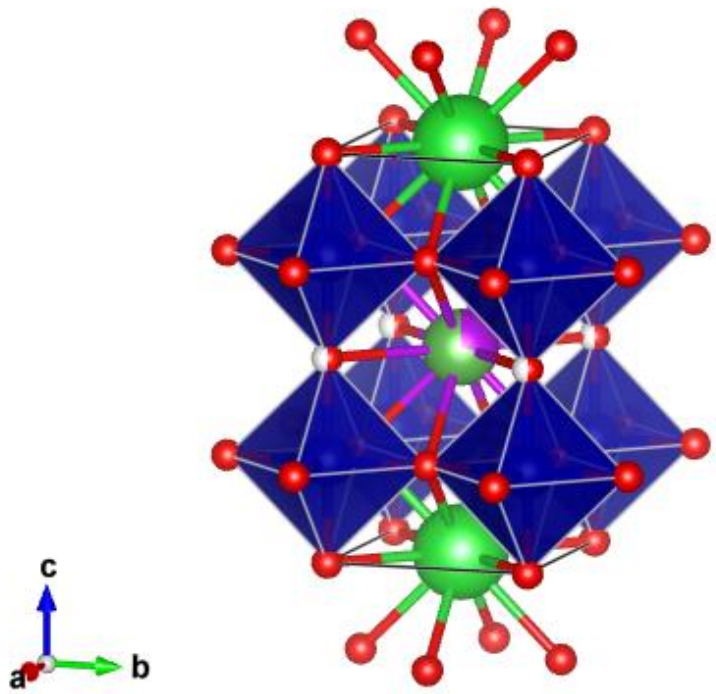

Figure 7 - VESTA model of BGLC37 with δ = 0.5. Ba = Green, Gd = Purple, La = Dark green, O = Red, Vacancy = White. Mixing of colours indicates mixed occupation of the site [23].

The oxygen stoichiometry of BGLC also varies with temperature and pO_2, which results in oxygen vacancies in the structure. These are compensated for by a variation in the oxidation

state of cobalt and tend to order themselves in the lanthanide layer due to an association between them and the lanthanide cations [24].

Ordering of vacancies and structure can also change with atmosphere and temperature. Since the gadolinium and lanthanum contents in BGLC will vary between compositions it is also worth considering how the outlier structures of BLC and BGC behave at different temperatures and oxygen partial pressures. In the case of BGC, vacancies will start to randomly form in the structure once the oxygen content per unit cell drops below 5. There are also additional phases that can form in low oxygen atmosphere, like the cubic disordered α-phase that forms for BGC at temperatures around 700 K in an inert atmosphere [25]. BLC on the other hand is more stable as a double layered perovskite at higher temperatures and lower pO_2. In highly oxidizing atmospheres and at lower temperature both the A-site and oxygen vacancy ordering becomes disordered. This is due to the layered double perovskite only being more stable when it does not have to compensate for vacancy formation [26].

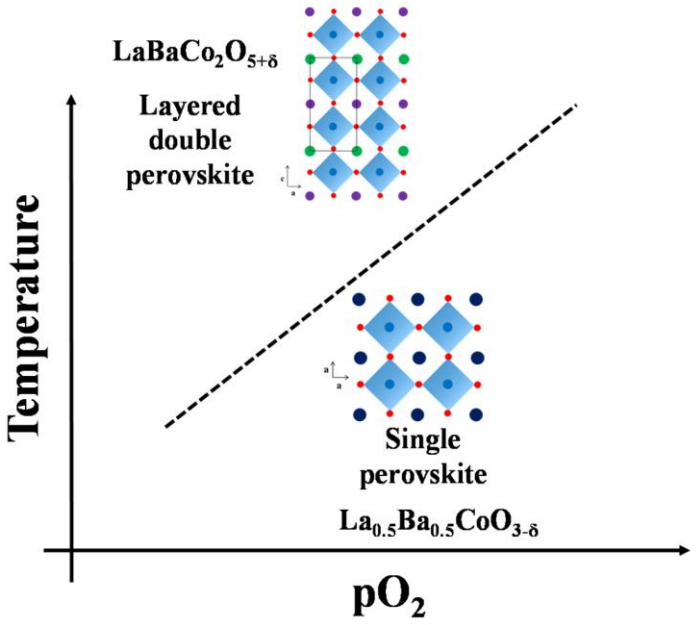

Figure 8 - Schematic stability diagram for BLC as a function of temperature and pO_2. [26]

3.2 BGLC as a PCEC electrode material

While proton ceramics have shown promise as electrolysers in labs, they have mostly been small scale button cells with low efficiencies of around 50% and have suffered from problems with conduction due to anode instability in steam. BGLC however is showing promise in this

regard and have already seen some testing as an anode material in a functioning PCEC. In a paper published by Vøllestad et.al in 2019, they investigated the performance of a tubular cell using a support of nickel and a Y-doped $BaZrO_3$-$BaCeO_3$ solid solution (BZCY) as cathode, BZCY as the electrolyte, and BGLC compositions with lanthanum substitution of barium ($Ba_{1-x}Gd_{0.8}La_{0.2+x}Co_2O_{6-\delta}$) as the anode (see Figure 9).

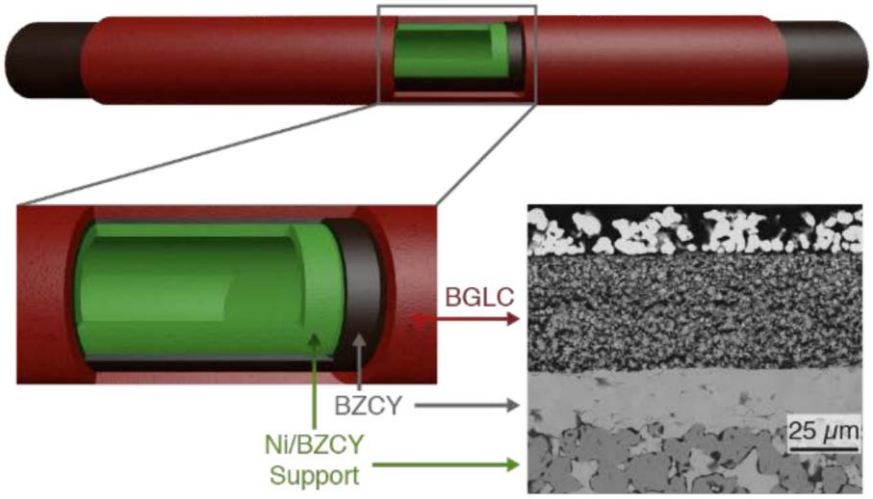

Figure 9 - Illustration of a tubular PCEC with an SEM picture showing the microstructure of a polished cross section of the tube [11].

In a cell like this the ceramic tube is encased within a closed reactor, where water vapor can be passed over the outside of the tube, while hydrogen gas is produced on the inside of the tube. This geometry also allows one to use the heat from compressing the hydrogen to drive the endothermic electrolysis reaction at the cathode. It was also found that BGLC tended to precipitate a $BaCoO_3$ secondary phase when exposed to 1.5 bar of steam, and that substituting 50% of the barium with lanthanum would counteract this effect. Thermal expansion and mismatching thermal expansion coefficients (TEC) between the BZCY and BGLC caused the anode to delaminate. To counteract this, a composite of BZCY and BGLC was used as anode, which improved the adhesion between the layers, and reduced the electrode polarization resistance from 4 to 0.8 Ωcm^2 at 600 °C. While a cell-level electrical efficiency of over 80% was reached at current densities of 150 mA/cm^2, it was between 60-70% when considering the vaporization energy and heat demand of the process. The limiting step for the water splitting reaction at the anode was attributed to surface related processes like diffusion, adsorption and dissociation. The study highlights the potential of BGLC as an anode material for PCECs with its high efficiency and stability in steam, but also a need for surface kinetics to be improved [11].

4 Experimental methods

4.1 Synthesis and characterization

To study how the kinetics of surface exchange vary with La and Gd content, five different compositions of BGLC were made, 19, 37, 55, 73 and 91. A sol-gel synthesis path was selected, as its precursors more easily result in an accurate stoichiometry, compared to a purely solid state synthesis where water content in the lanthanide oxides can vary due to their hygroscopic nature.

$La(NO_3)_3 \cdot 6\ H_2O$, $Gd(NO_3)_3 \cdot 6\ H_2O$, $BaCO_3$ and $Co(CH_3COO)_2 \cdot 4\ H_2O$ were selected as precursors due to their solubility, with citric acid as a complexing agent for the gel. In each round of synthesis, 10 g of the selected composition was made, with appropriate amounts of precursor calculated. The amount of citric acid was based on a 2:1 ratio of citrate to cations, estimated to about 30 g. After weighing the correct amounts of precursor, 75mL of distilled water was added to a 1 L beaker on a heating plate set to 50 °C with stirring. The citrate was then dissolved, before gradually adding barium(II)carbonate to avoid violent foaming from the CO_2 generated by solution of the carbonate. Lastly, the nitrates and cobalt(II)acetate were added. Once dissolved the beaker was wrapped in some aluminium foil to retain heat and the heating plate was turned up to 250 °C. Once the solution was reduced enough to start forming a gel, the beaker was removed, covered with a watch glass, and left in a ventilated heating cabinet at 250 °C overnight to dry and decompose most of the nitrate. This resulted in a spongy, low density xerogel as pictured in Figure 10, that was lightly compressed to reduce volume, before transferring it to an alumina crucible.

Figure 10 – Xerogel for BGLC synthesis after drying the mixed precursors at 250 °C.

To remove leftover carbon and nitrates the powder was then slowly heated to 600 °C in a ventilated furnace with a rate of 60 °C/hr and left for 4 hours. After that there are few volatile compounds left, and the powder can safely be heated to 1000 °C at a rate of 250 °C/hr and left for 32 hours to calcinate.

Once the calcination was done, the powder was analysed with XRD on a Bruker AXS D8 Discover. The resulting spectra were imported to DIFFRAC.EVA and compared to existing BGLC compositions from Crystallography Open Database and previous synthesises to assess the phase purity. The five batches were then sieved into grain size intervals with diameters of >125 µm, 125-63 µm, 63-45 µm and <45 µm. The morphology of each sample was then investigated with a scanning electron microscope (SEM). Once each composition had been imaged, a sample of BGLC19 and BGLC73 with grain diameters of 63-45 µm was sent to BET analysis to examine the specific surface area.

4.2 Gas Phase Analysis

In the GPA experiment a setup was used consisting of two vacuum pumps, a pressure gauge, a quartz reaction tube, a mass spectrometer, and a rollable high temperature furnace (see Figure 11).

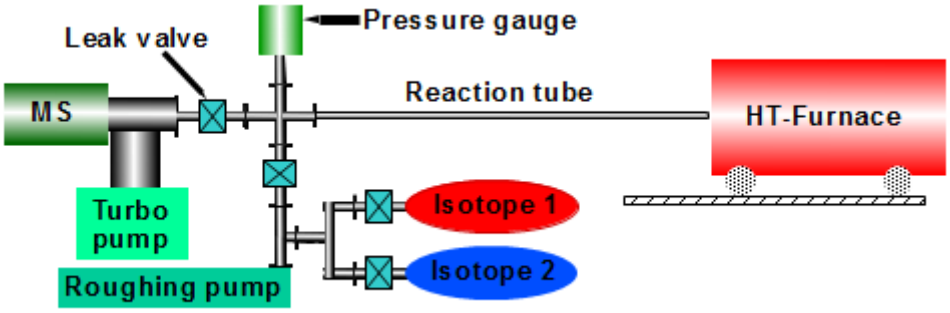

Figure 11 - Schematic of a GPA setup [27].

A sample of BGLC19 of was weighed and placed in a small quartz boat and placed inside the reaction tube. The tube was then put under vacuum, and an atmosphere of 20 mbar of oxygen added. While there is some ^{18}O present in the oxygen used for annealing, the amount is negligible. The sample was then heated to 400 °C in the tubular furnace and left to anneal overnight for about 16 hours. Then the furnace was rolled away from the tube, before quenching the reaction tube by running some water over it and leaving it to cool outside the furnace for about 30 minutes. After this the gas was vacuumed from the reaction tube and the atmosphere replaced with 20 mbar of $^{18}O_2$. The valve between the reaction chamber and the mass spectrometer was then opened to allow some of the gas to slowly leak through, the furnace rolled back to the reaction tube, and the measurement started. Through the experiment the masses tracked were 32, 34 and 36, corresponding to the three possible combinations of oxygen isotopes. After roughly two hours the sample reached equilibrium and the data could be analysed by running a script based on Boukamp's approach in Equation 14 [28].

4.3 Pulse Isotope Exchange

The core of the PIE setup is the reaction chamber, consisting of a 2 mm inner diameter quartz tube in a tubular furnace and a mass spectrometer. Its gas delivery system is however a little

more complex than for GPA, as it must handle a constant flow of the carrier/annealing gas, a wetting stage, and filling and releasing the loop of the pulse gas.

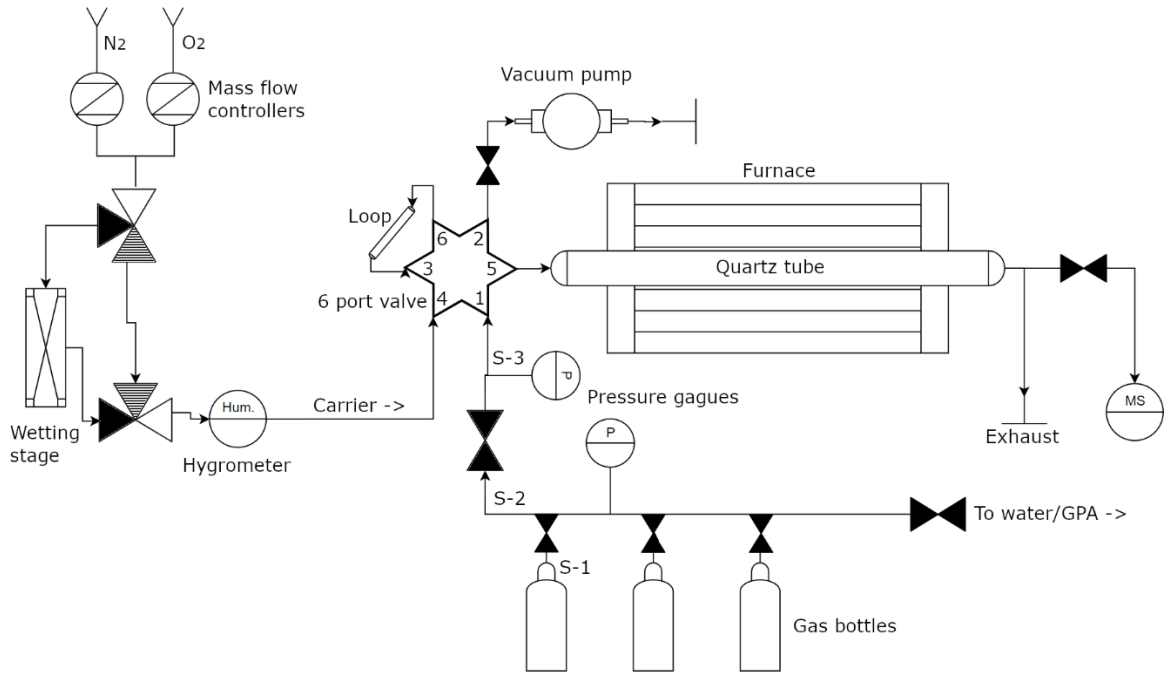

Figure 12 - Illustrated layout of the gas lines in the PIE setup. Double and triple triangles are 2- and 3-way valves.The output of the 3-way valves can also be toggled between the black and striped triangles. Stage 1-3 are denoted by S1, S2 and S3. The schematic was designed using Visual Paradigm Online [29].

The digital mass flow controllers (MFC) and the mass spectrometer are connected to a computer, allowing us to set up the gas flow and run measurements from it. The 6-port valve is electronically controlled by a button to switch between states, while the 2- and 3-way valves are operated manually. Additionally, the stage-2 between the gas bottles and the 6-port valve can be opened to a series of vials containing four different isotope mixes of water, and the GPA setup, allowing us to use the roughing and turbo pumps for emptying the lines if needed (see Figure 12). The 6-port valve allows us to fill the pulse loop from stage-2 or empty it via the vacuum pump, while still feeding the reaction chamber with the carrier gas while it is in position A. When the pulse is ready to be sent, a switch to position B routes the carrier gas through the pulse loop to transport it into the reactor (see Figure 13).

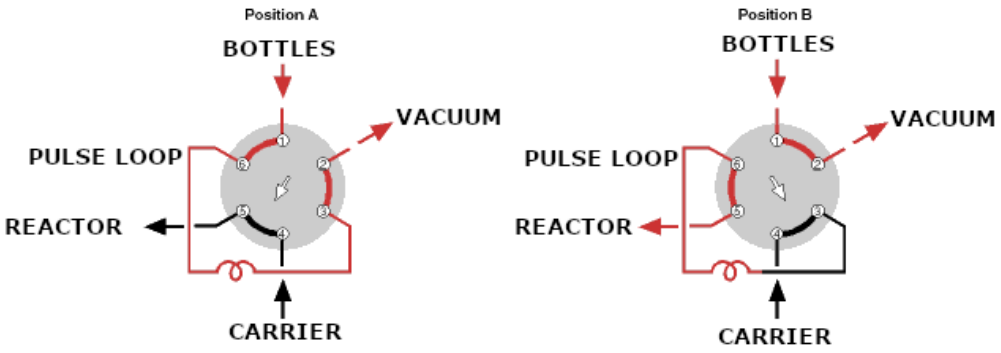

Figure 13 - Illustration of the 6-port valve and its connections in the two different states [30].

When preparing the sample, a piece of quartz wool is inserted into the quartz tube close to the middle of the tube. The sample is then weighed and carefully funnelled into the tube so that it resides in the middle, which will be situated in the heating zone. Another piece of quartz wool is inserted on the other side and lightly compressed against the sample with an alumina rod. The quartz tube is then inserted into the furnace and connected to the gas lines on both sides. Once in place the sample is ready for annealing. First the mass flow controllers are set to their correct flows via the desktop software. A total flow of 50 mL/min was used in all experiments, so in experiments using 2% oxygen, the MFCs were set to 49 mL/min of nitrogen and 1mL/min of oxygen. In all experiments, except for one, the sample was then pre-annealed overnight at 850 °C for 5 hours, before cooling down to 550 °C at a rate of 250 °C/h to await measurement. Measurements were performed with steps of decreasing temperature.

Before measurements stage 2 is, unless already prepared, filled with the designated pulse gas mix from one of the bottles by pressurizing stage 1, closing the bottle, and opening the valve between stage 1 and 2 to avoid overfilling. The pulse loop can then be filled as close as possible to 1000 mbar by opening the valve between stage 2 and 3 if the 6-port valve is in position A. The leak valve to the mass spectrometer can then be opened, the recording program started, and the pulse sent. Once the measurement is over, the 6-port valve is switched back to position A and the loop can be emptied and re-filled before cooling to the next temperature step. A time window of 15 minutes to 2 hours was used between measurements to allow the sample to equilibrate, depending on temperature. Temperature steps of 25 °C were used between 550-350 °C and steps of 50 °C between 350-250 °C in most experiments.

In the oxygen experiments pre-made gas mixes of dry 2% and 21% ^{18}O in argon were used, and the masses tracked were 36 ($^{18}O_2$), 34 ($^{18}O^{16}O$), 32 ($^{16}O_2$) and 40 (Ar). A chamber pressure

of 1×10^{-6} mbar was used in the MS, running a secondary electron multiplier detector. Argon is measured to be used as a calibration of the pulse volume, as the filling of the loop is not always precise. Once a data set for a given composition was finished, it was processed by a Matlab script by V. Thoréton together with other necessary parameters like specific surface area, mass and p_{O_2} to calculate the activation energies and surface exchange coefficients [31].

In the experiments with water vapor, a custom gas mix had to be made. This was done by vacuuming the line from an open gas bottle, via stage 1 and 2, to the water vials. Once under vacuum, a vial containing D_2O was opened to fill the line and bottle with heavy water vapor to about 16 mbar. After some calculations to design a final gas mix of 5 bar, the correct partial pressures of the other gases were added via stage 2 to make a final blend consisting of 0.3% D_2O, 1.0% He, 2.0 % $^{16}O_2$ and 96.7% N_2. Argon was not used in this mix, as we want to track mass 20 (D_2O), and Ar^{2+} would be picked up by the MS as mass 20. The water exchange experiments were performed almost identically to the ones with oxygen, but a Faraday detector with a chamber pressure of 1×10^{-4} was used instead of a secondary electron multiplier for the mass spectroscopy. Additionally, the carrier/annealing gas was humidified by running the carrier gas through a wetting stage consisting of a Nafion™ tube partially submerged in type 2 water. Achieving an accurate p_{H_2O} with this method is somewhat challenging as it depends on temperature and the degree of submersion, but a consistent 16 mbar (1.6 % at ambient pressure) was achieved for both measurements.

5 Results and discussion

5.1 Sample characterization

After synthesis all compositions were shown to have good phase purity by the absence of any large, unexpected peaks in the XRD spectra (example in Figure 14).

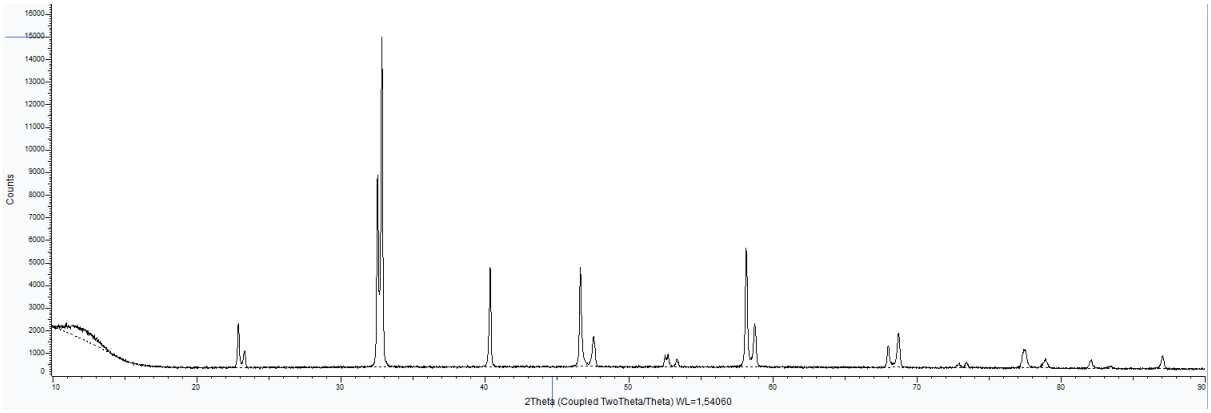

Figure 14 - X-ray diffractogram of BGLC37.

Once these had been sieved into their designated particle size intervals, each sample was examined with SEM to study their morphology.

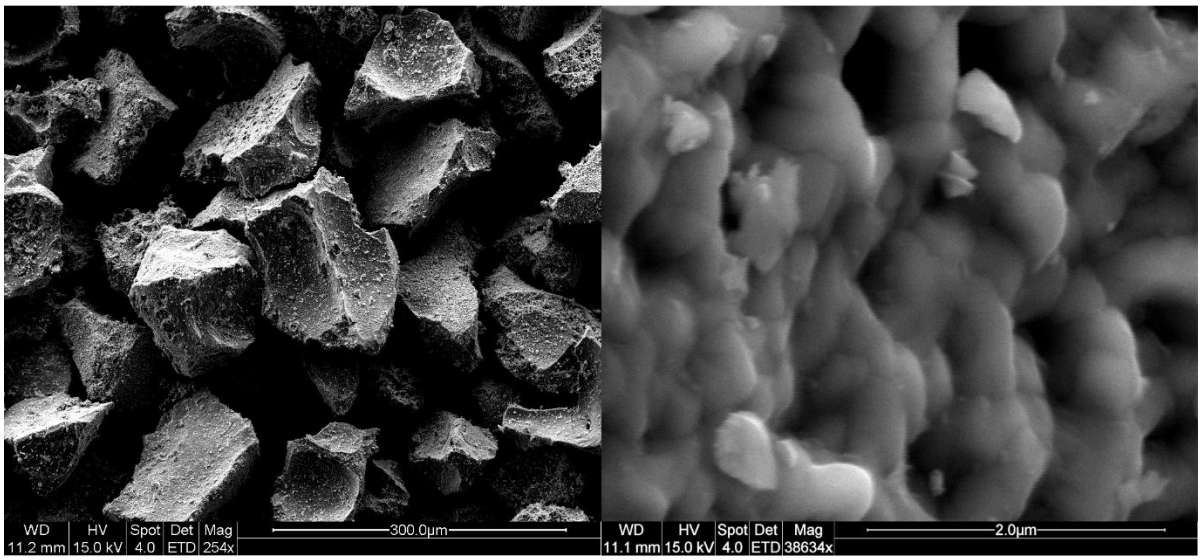

Figure 15 - Secondary Electron SEM image of BGLC19 grains at 250x and 40.000x magnification.

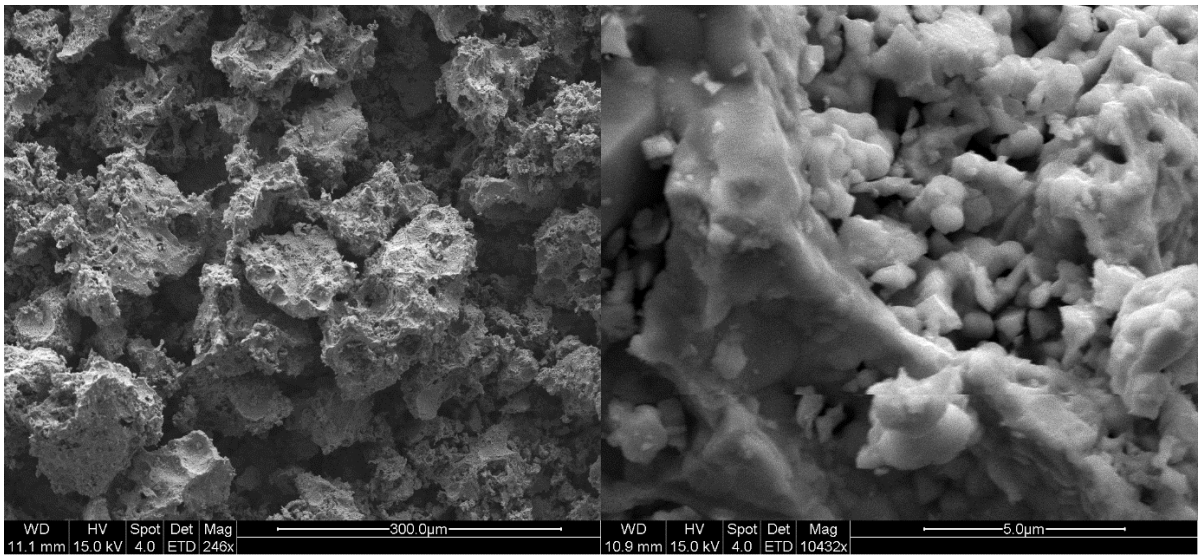

Figure 16 - Secondary Electron SEM image of BGLC73 grains at 250x and 10.000x magnification.

As seen from the images in Figure 15 and Figure 16, the morphology of BGLC19 and 73 composition varies from relatively smooth to containing many smaller grains on the surface. From this one could expect a big gap in specific surface are. A quick geometrical example shows that any flat area covered by a hemisphere will have twice the surface area comparatively.

$$\frac{A_{h.sphere}}{A_{circle}} = \frac{2\pi r^2}{\pi r^2} = 2 \tag{20}$$

To numerically compare the specific surface area of these two compositions, they were analysed with BET at SINTEF in Oslo. The results in Table 4 show that the specific surface area and pore size of both compositions are very close to each other.

Table 4 - Summarized data from BET analysis of BGLC19 and 73.

Composition	**Specific surface area (m^2/g)**	**Mean pore diameter (nm)**	**Total pore volume (cm^3/g)**
BGLC19	0.39	23.5	0.0023
BGLC73	0.37	19.8	0.0018

Surprisingly BGLC19, with a seemingly more even macro surface, has a higher specific surface area than BGLC73. The pore diameter and volume suggest that the morphology at nanoscale is more significant for the specific surface area than what SEM pictures can show us. A surface

area around 0.38 m^2/g is relatively low, but not too far from what could be expected from ceramic beads (0.1-1.1 m^2/g). [32] This could be attributed to the long calcination time of the samples allowing a higher degree of sintering of the powder.

5.2 Pre-annealing and surface layers

The goal of the first PIE runs was to test the behaviour of the material and to determine the temperature range measurements are best carried out at. As the samples had been stored in containers closed with plastic caps for several months between synthesis and measurement, there was a concern that the samples had developed a passivating hydroxide or carbonate layer. To examine this a test run was set up to heat the sample to 500 °C in the PIE setup, with a nitrogen flow of 50 mL/min.

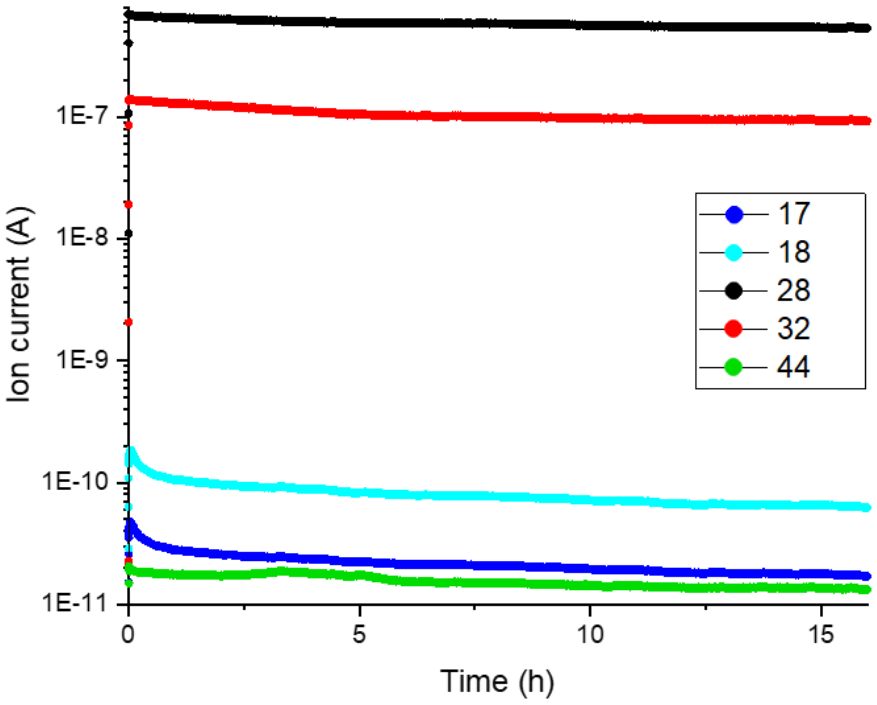

Figure 17 - Ion currents of OH (17), H20 (18), CO (28), O2 (32) and CO2 (44) in inert atmosphere after heating to 500 °C.

From the graph in Figure 17 we can see that the amount of gas emitted from the sample is very low, with CO and O_2 dominating. This could indicate a small passivating layer of carbonate that is decomposed to CO in the inert atmosphere. One way to combat this is pre-annealing the sample.

In order to test the difference between pre-annealing and running samples from room temperature, an experiment was set up measuring the oxygen exchange rate of BGLC19 with temperature steps starting at room temperature, and while cooling after a 5-hour resting period at 850 °C. A constant 50 mL/min flow of synthetic air (p_{O2} = 0.21) was applied, while a gas mix of 21% $^{18}O_2$ in argon was used as the pulse. From the data in Figure 18 and Figure 19 we can see that the surface exchange coefficient is slightly lower for the un-annealed sample at 400 °C, with a higher activation energy. Looking specifically at the activation energies and surface exchange coefficients for both the total exchange process and adsorption and incorporation in Table 5, it shows that the un-annealed sample has a lower incorporation energy and much higher adsorption energy.

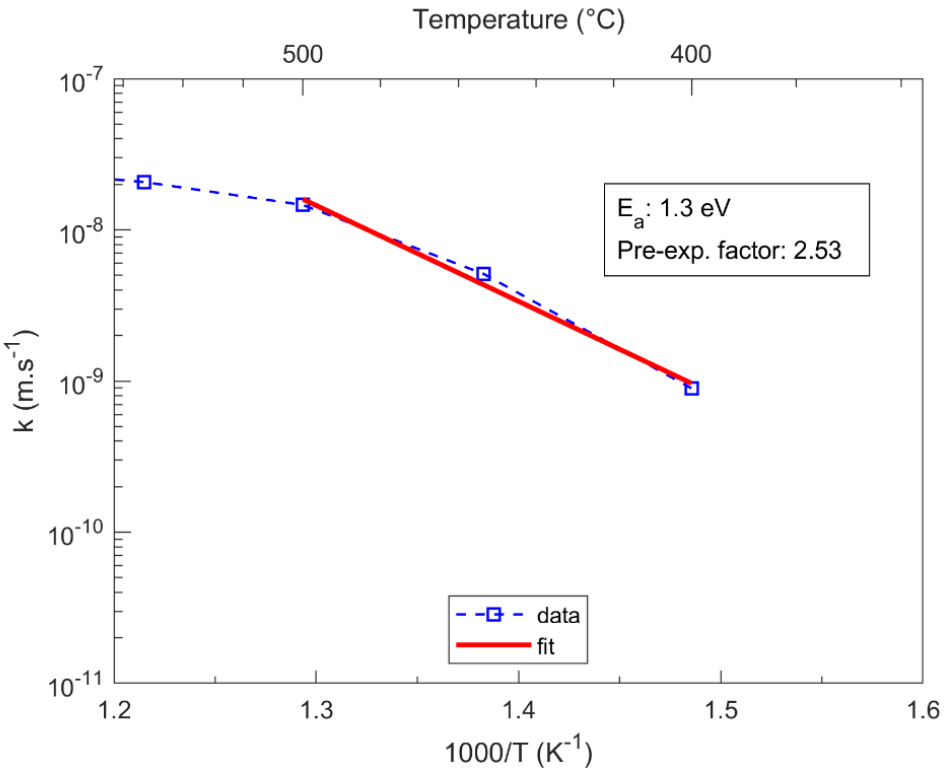

Figure 18 - Arrhenius plot of surface exchange rates of oxygen for BGLC19, measured at increasing temperatures without pre-annealing.

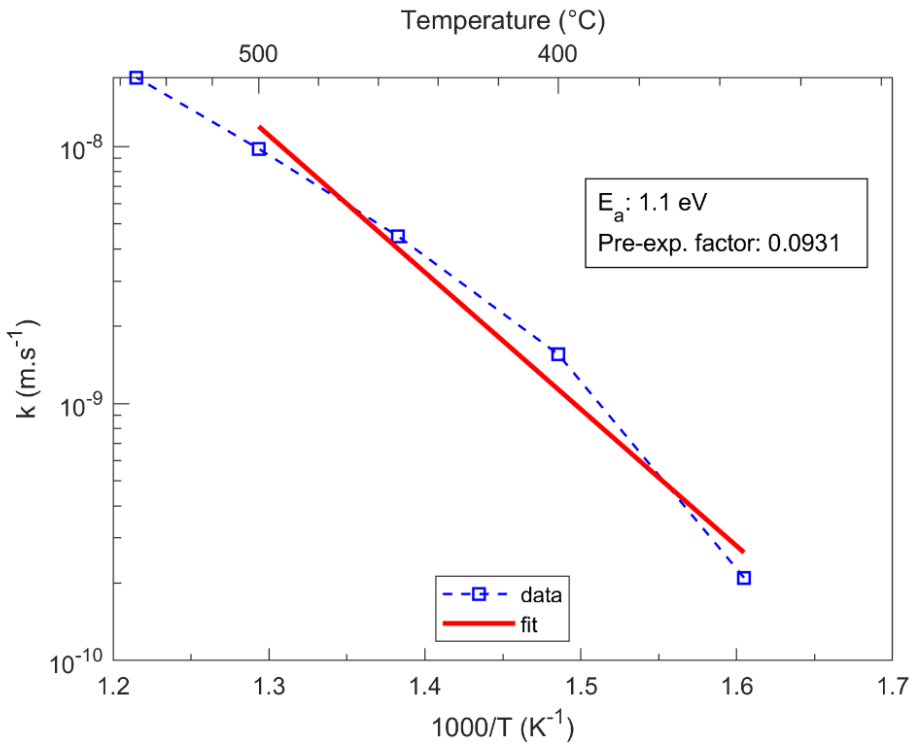

Figure 19 – Arrhenius plot of surface exchange rate of oxygen for BGLC19, measured at decreasing temperatures after pre-annealing.

Table 5 - Activation energies for total exchange, adsorption and incorporation, and exchange coefficient at 400 °C. E_{ads} for the up run is not realistic, and caused by a single outlying data point.

Run type	**E_0 (eV)**	**E_{ads} (eV)**	**E_{inc} (eV)**	**$\Re_0$ @ 400 °C (mol m^{-2} s^{-1})**
Up	1.3	9.1	0.67	3.9×10^{-5}
Down+annealing	1.1	0.62	1.1	6.8×10^{-5}

When looking closer at the data for the un-annealed sample there is one outlying data point at 500 °C in Figure 20 for the adsorption energy that makes the linear regression jump wildly from the trend otherwise. In the raw data in Figure 21 we can see that the curve for release of $^{16}O^{18}O$ doesn't spike anymore and rather tapers slowly off over the course of a minute. This indicates that the sample wants to retain oxygen, possibly to replace removed carbonate from the surface. Many signs point towards the formation of a surface layer during storage that starts decomposing at around 500 °C. With these findings, every subsequent measurement was performed with a pre-annealing and decreasing temperature steps.

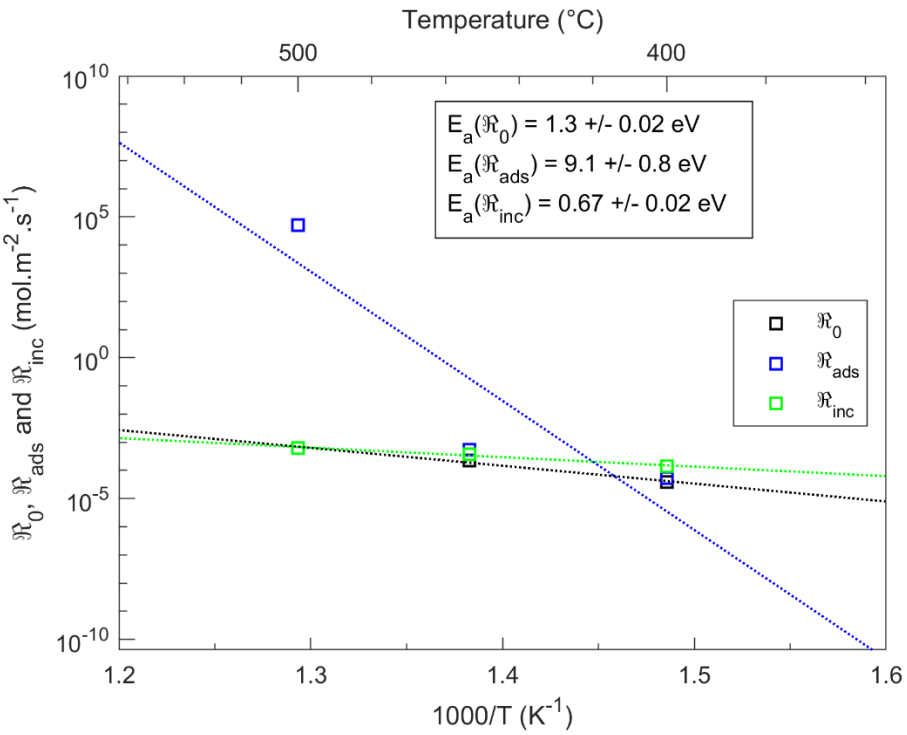

Figure 20 - Rates and activation energies for un-annealed BGLC19 measured at increasing temperature steps.

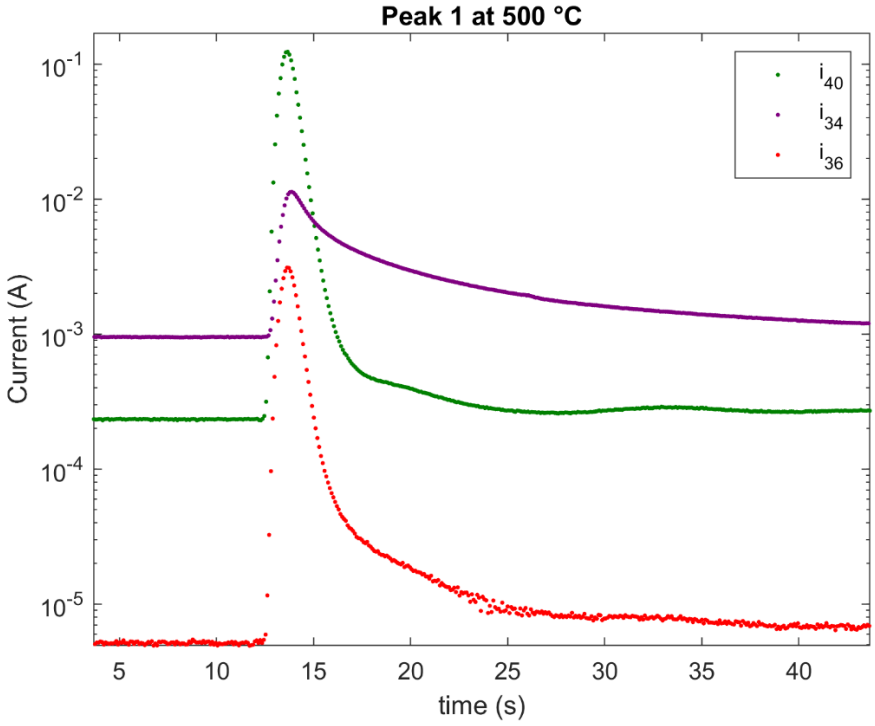

Figure 21 - Mass spectroscopy raw data for BGLC19 at 500 °C measured at increasing temperatures without pre-annealing

5.3 Varying pO_2

As oxygen 18 is a relatively expensive isotope, using a gas mix of 2% $^{18}O_2$ in Argon instead of 21% would cut the usage of the isotope tenfold over all experiments. Additionally, there is some experience in the Electrochemistry group with less oxygen giving cleaner and more reliable PIE data. This lead to an investigation of the effects of changing the partial pressure of oxygen.

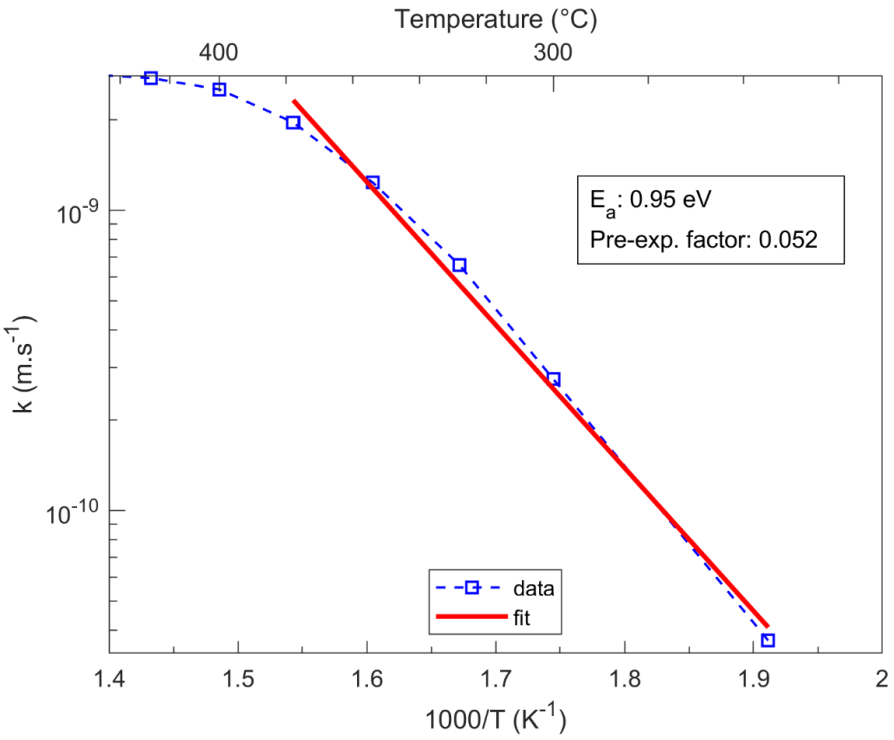

Figure 22 - Arrhenius plot of surface exchange rates of oxygen for BGLC19 in 2% oxygen atmosphere, measured at decreasing temperatures after pre-annealing.

Compared to higher oxygen partial pressures, the data points in Figure 22 follow each other in a clearer trend, while also staying linear all the way down to 250 °C (the last temperature step before a final room temperature measurement). The slope tapering off at around 400 °C and upwards could be due to a change of activation energy between high and low temperature regimes.

Table 6 - Activation energies for total exchange, adsorption and incorporation, and exchange coefficient at 400 °C.

Run type	**E_0 (eV)**	**E_{ads} (eV)**	**E_{inc} (eV)**	**$\Re_0$ @ 400 °C (mol m^{-2} s^{-1})**
21% O_2	1.1	0.62	1.1	6.8×10^{-5}
2% O_2	0.84	0.79	1.1	1.2×10^{-4}

Surprisingly the energy for incorporation, compared between the two gas mixes in Table 6, remains unchanged. A decrease in oxygen partial pressure might lead to more oxygen vacancies, and thus a lower barrier of incorporation could have been a possibility. An increase in adsorption energy is however as expected due to the presence of fewer oxygen molecules in the atmosphere, and on the surface, making adsorption more favourable. Given the results it was deemed acceptable to use a lower p_{O_2} for subsequent measurements.

5.4 Variations across compositions

So far, we have only been looking at a single composition of BGLC, but as mentioned the goal was to test 5 of them to compare their performances. For these experiments a constant 50 mL/min flow of 2% oxygen in nitrogen was used, with pulses of 2% $^{18}O_2$ in argon, 5-hour pre annealing at 850 °C and decreasing temperature steps.

Table 7 - Summary of exchange energies and surface exchange coefficients for BGLC19-BGLC91.

Composition	**E_0 (eV)**	**E_{ads} (eV)**	**E_{inc} (eV)**	**$\Re_0$ @ 400 °C (mol m^{-2} s^{-1})**
BGLC19	0.84	0.79	1.1	1.2×10^{-4}
BGLC37	0.88	0.87	0.93	6.4×10^{-5}
BGLC55	0.91	0.92	0.82	5.8×10^{-5}
BGLC73	0.62	0.69	1.1	1.1×10^{-4}
BGLC91	0.8	0.75	1.3	1.1×10^{-4}

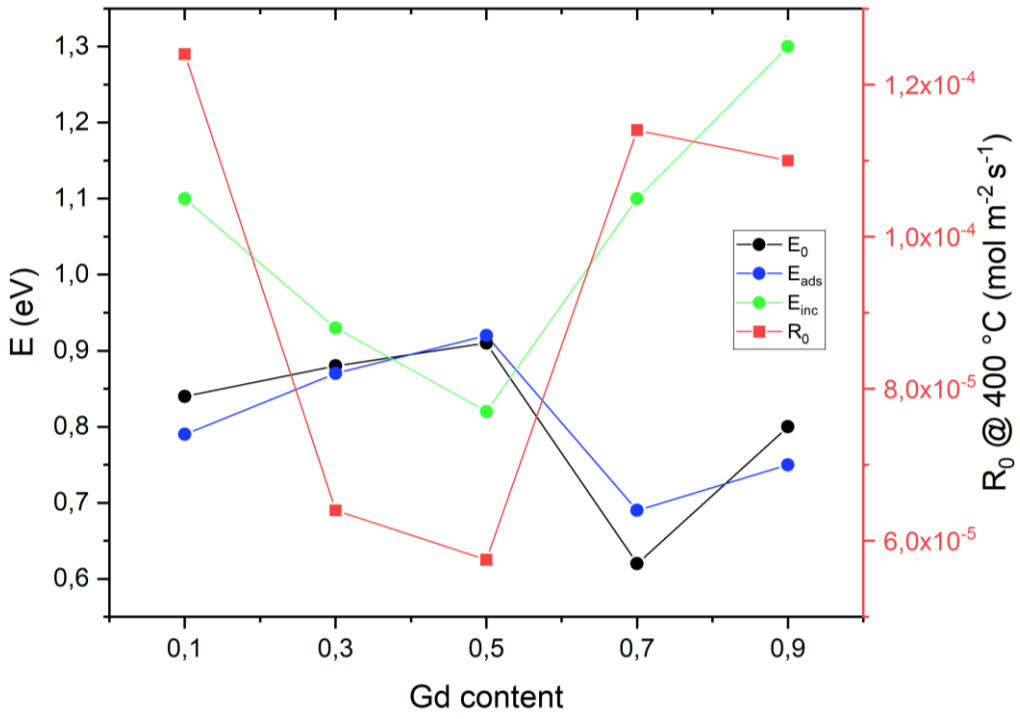

Figure 23 - Summary of exchange energies and surface exchange coefficients for BGLC19-BGLC91. A Gd content of 0.3 corresponds to BGLC37 etc.

From the summary of the experiments across compositions in Table 7 and Figure 23, we see a notable dip in the surface exchange rate for BGLC37 and BGLC55, while the activation energies are at their highest. For BGLC73 and BGLC91 on the other hand, we see much lower energies for adsorption, and higher surface exchange coefficients than the two previous compositions. BGLC19 deviates somewhat from the trend, by having the highest exchange rate, but slightly higher activation energy and adsorption energy. The incorporation energy is also of note, as it is at its lowest for BGLC55, and increases towards both higher and lower gadolinium content. The maximum reaction rate also flattens out at around 450 °C for most compositions as seen in Figure 24. At this point the rate could be limited by other factors such as flow rates in the chamber or the amount of available gas for exchange.

It is likely that vacancy concentrations play a significant role in the kinetics of these experiments. BGLC contains less oxygen vacancies with higher lanthanum content [13]. Due to this it is possible that low Gd content results in fewer oxygen vacancies, and conversely a higher incorporation energy. With higher Gd content, it might be desirable to form vacancies,

and filling them might not be energetically favourable, also leading to a higher incorporation energy.

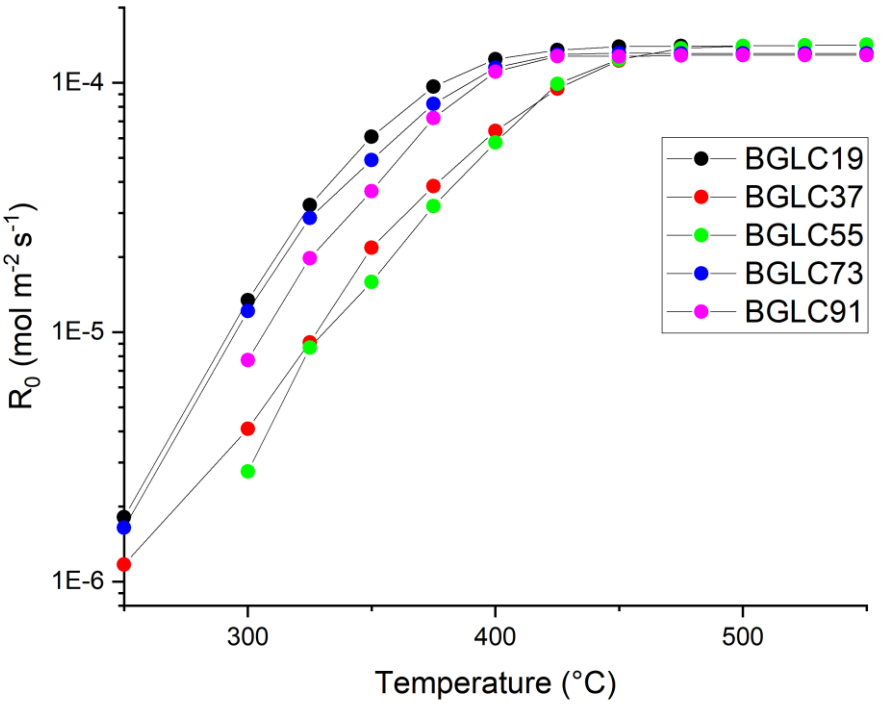

Figure 24 - Surface exchange rates for all BGLC compositions in 2% oxygen atmosphere at ambient pressure across all measured temperatures.

Considering both activation energy and surface exchange rate, gadolinium content somewhere between 0.7 and 0.9 is likely optimal in terms of oxygen exchange. For use in PCECs the higher incorporation energy is positive as the likelihood of desorption before incorporation becomes higher.

5.5 Comparison to GPA

Before the introduction of the PIE instrument, the initial plan of the project was to use GPA measurements to find the surface exchange energies. Some of the early tests with BGLC19 were also performed with this method. While PIE and GPA are similar, GPA is slower and is performed with a much larger reaction chamber.

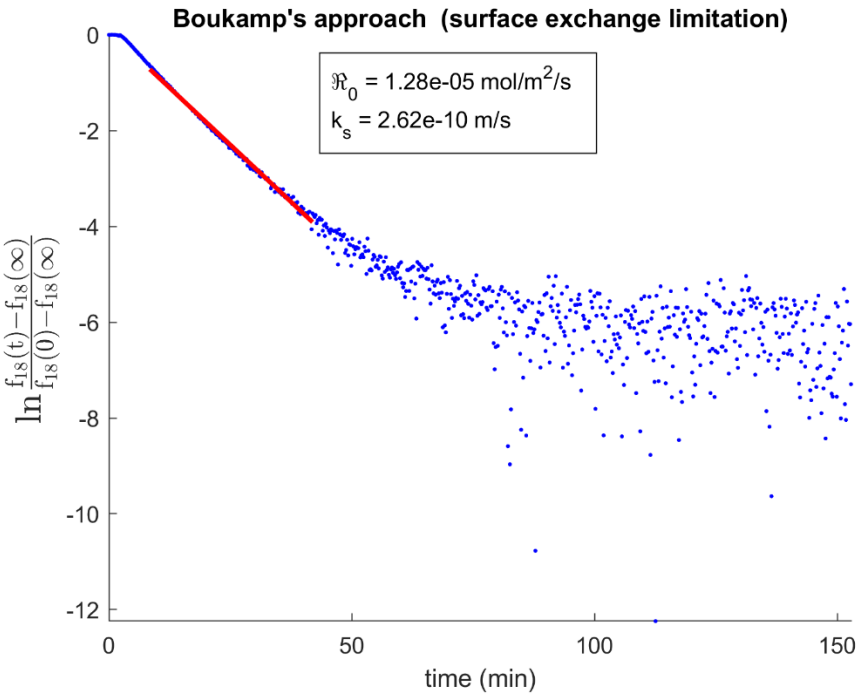

Figure 25 - GPA measurement of BGLC19 at 400 °C in 21% oxygen atmosphere at ambient pressure.

The calculated surface exchange coefficient is about an order of magnitude lower than what the PIE yields. This suggests that the measurement is not necessarily limited by the surface reaction, but rather the gas transport in the chamber as there is no active flow. With the current setup for GPA in the lab it is not suited for working on powder samples of BGLC, while the possibility of using pellets with lower surface area remains open.

5.6 Water exchange

The exchange and adsorption of water is another key property of PCEC anodes. To test the kinetics for water adsorption an experiment was designed to use D_2O as a tracer isotope in the PIE. With the current setup it was only possible to make a gas mix carrying around 0,3% D_2O, meaning a p_{D_2O} of about 3 mbar. As the only method of adding water to the constant gas flow was by passing the gas through a Nafion™ tube partly submerged in water, getting a similar p_{H_2O} proved to be difficult. As such measurements were not performed at chemical equilibrium, as the samples were exposed to about 16 mbar of water.

During the experiments no mass 20 was recorded by the mass spectrometer, despite running with a Faraday detector with a chamber pressure of about 1×10^{-4} mbar, three orders of

magnitude above what was used with the SEM detector in the oxygen experiments. This indicates that none or very little D_2O was reaching the instrument. There was however a clear peak of mass 19, indicating DHO, with a constant presence of 18 (H_2O or DO^-) and 17 (OH^-) as seen in Figure 27. This could indicate that the ratio of H_2O to D_2O is large enough for most of the deuterium to be exchanged to water molecules, forming semi-heavy water. With the available data there is no good way of calculating surface exchange ratios in the same way as oxygen. We can however integrate the peaks of mass 19 to see if there is a noticeable difference between two compositions.

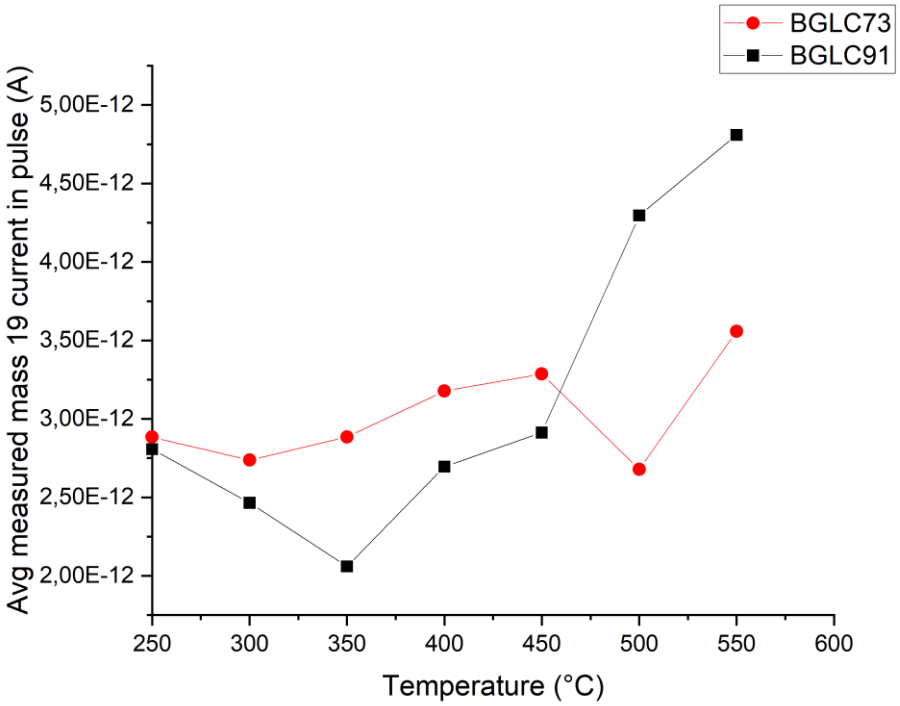

Figure 26 - Total measured charge of mass 19 peaks averaged by the integrated time interval.

A qualitative look at the data in Figure 26 might suggest that BGLC91 exchanges more water than BGLC73 at temperatures above 450 °C, however there are no clear trends, and there is a significant degree of variability in the data set. One interesting aspect of the water containing pulses is that they take more time to reach the detector, compared to the oxygen experiments (see Figure 21 and Figure 27). This could be due to adsorption of D_2O on the surface of the sample, and if the adsorption energy is relatively high it might take more time for the gas to desorb and reach the MS. Still the data remains inconclusive for the time being. If one could accurately reach higher vapor pressures in both the annealing gas and pulse gas, we could be able to find a similar relationship between composition and water exchange as with oxygen.

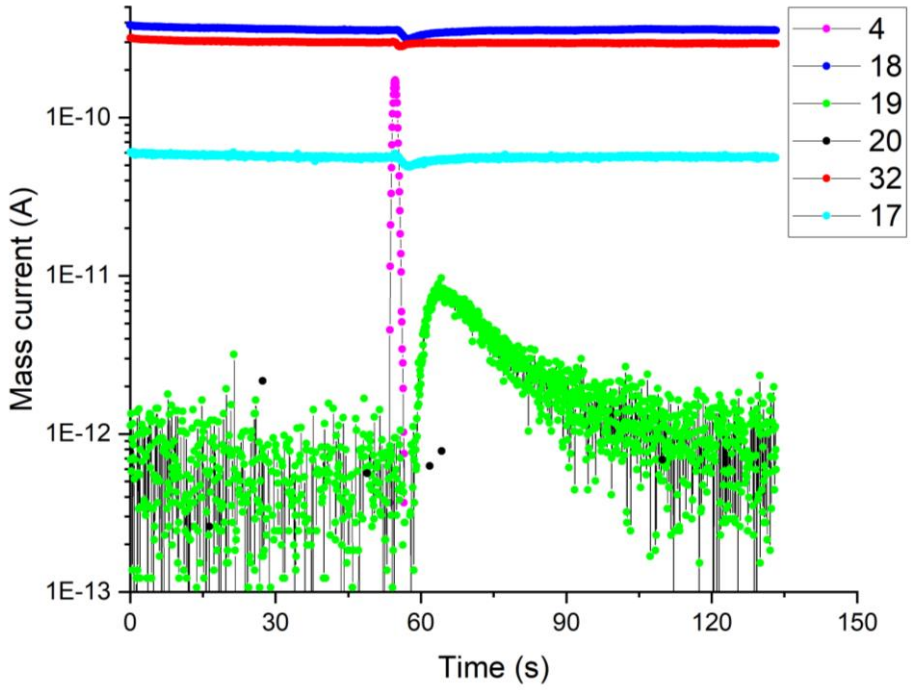

Figure 27 - Mass currents for BGLC91 while recording a pulse containing 0,3% D_2O at 450 °C in a 2% oxygen and 1.6% water atmosphere at ambient pressure.

5.7 Future work

While this project reveals some of the surface properties of BGLC, it is far from complete. Experiments for all compositions with more p_{O_2} values could be able to give a p_{O_2} dependency of the surface kinetics for varying BGLC composition. Compositions with substitution of barium have not been considered in this project, and kinetic data from them would give a more complete image of BGLC's surface properties. A more in-depth study of the morphology, oxygen vacancy concentration, and possible secondary phases formed during the experiments would be useful to supplement the discussion about the variation in exchange rate between compositions. Ab initio modelling is also a powerful tool that could give us information about the activation energies for reaction steps experimental measurements struggle to measure, like energy barriers for surface diffusion, which can be estimated through nudged elastic band calculations. Lastly more work is required to produce good results involving water vapour. Water surface kinetics is an important part of a PCEC anode and might be the deciding factor for finding the BGLC composition most suited for practical application.

6 Conclusions

Based on the PIE measurements performed in this project, there are some indications that long term storage of BGLC in air could be detrimental to the surface kinetics of the material due to exposure to water vapor and CO_2 over time. By annealing powders in dry air surface layers of carbonates and hydroxides can be removed, but it is unclear how it would affect the morphology of a dense sample. The oxygen exchange experiments indicate that compositions with a higher gadolinium content have faster surface exchange with lower activation energies, with BGLC73 being notably lower. BGLC19 deviates somewhat from this trend by having higher surface exchange coefficients than BGLC73, but a higher adsorption energy makes it less ideal for PCEC purposes. While the data from the experiments with water exchange could suggest that BGLC73 performs better than BGLC91 up to 450 °C, the data did not allow for the extraction of surface exchange coefficients or activation energies. With no clear trends otherwise, the data for water exchange remains inconclusive.

Using PIE for evaluating the kinetics of powder samples have shown itself to be a powerful tool, being able to collect data quicker compared to GPA, and with higher precision for materials with fast exchange rates. While the current setup for measurements involving water might not be optimal, it shows promise for future iterations.

7 References

[1] Our World in Data, "Solar PV module prices." https://ourworldindata.org/grapher/solar-pv-prices (accessed 21/6, 2021).

[2] IEA, "Batteries and hydrogen technology: keys for a clean energy future." https://www.iea.org/articles/batteries-and-hydrogen-technology-keys-for-a-clean-energy-future (accessed 10/7, 2021).

[3] R. Matulka, "The History of the Electric Car." *Department of Energy.* https://www.energy.gov/articles/history-electric-car (accessed 10/7, 2021).

[4] EV Database, "Range of full electric vehicles." *Electric Vehicle Database.* https://ev-database.org/cheatsheet/range-electric-car (accessed 10/7, 2021).

[5] A. Goede, "CO 2 -neutral fuels." *EPJ Web of Conferences,* 2015.

[6] K. Mazloomi and C. Gomes, "Hydrogen as an energy carrier: Prospects and challenges." *Renewable and Sustainable Energy Reviews,* 2012.

[7] Clean Energy Institute, "What is a lithium-ion battery and how does it work?" *University of Washington,* https://www.cei.washington.edu/education/science-of-solar/battery-technology/ (accessed 14/07, 2021).

[8] S. D. Ebbesen, S. H. Jensen, A. Hauch, and M. B. Mogensen, "High Temperature Electrolysis in Alkaline Cells, Solid Proton Conducting Cells, and Solid Oxide Cells." *Chemical Reviews,* 2014.

[9] M. A. Laguna-Bercero, "Recent advances in high temperature electrolysis using solid oxide fuel cells: A review." *Journal of Power Sources,* 2012.

[10] F. M. Sapountzi, J. Gracia, C. Weststrate, H. Fredriksson, and H. Niemantsverdriet, "Electrocatalysts for the generation of hydrogen, oxygen and synthesis gas." *Progress in Energy and Combustion Science,* 2017.

[11] E. Vøllestad *et al.*, "Mixed proton and electron conducting double perovskite anodes for stable and efficient tubular proton ceramic electrolysers." *Nature Materials,* 2019.

[12] T. Norby, "Defects and transport in crystalline materials." *University of Oslo*, 2015.

[13] E. Vøllestad, M. Schrade, J. Segalini, R. Strandbakke, and T. Norby, "Relating defect chemistry and electronic transport in the double perovskite Ba1−xGd0.8La0.2+xCo2O6−δ (BGLC)." *Journal of Materials Chemistry A,* 2017.

[14] D. Poetzsch, R. Merkle, and J. Maier, "Proton uptake in the H+-SOFC cathode material Ba0.5Sr0.5Fe0.8Zn0.2O3−δ: transition from hydration to hydrogenation with increasing oxygen partial pressure." *Faraday Discussions,* 2015.

[15] D. Poetzsch, R. Merkle, and J. Maier, "Stoichiometry Variation in Materials with Three Mobile Carriers-Thermodynamics and Transport Kinetics Exemplified for Protons, Oxygen Vacancies, and Holes." *Advanced Functional Materials,* 2015.

[16] A. J. Bard, and L. R. Faulkner, "Electrochemical methods : fundamentals and

applications." *2nd ed. New York, Wiley*, 2001.

[17] R. Strandbakke *et al.*, "Gd- and Pr-based double perovskite cobaltites as oxygen electrodes for proton ceramic fuel cells and electrolyser cells." *Solid State Ionics,* 2015.

[18] X. Zhu, and W. Yang, "Mixed Conducting Ceramic Membranes : Fundamentals, Materials and Applications."*1st ed. Berlin, Springer*, 2017.

[19] B. Boukamp, I. Vinke, K. Devries, and A. Burggraaf, "Surface oxygen exchange properties of bismuth oxide-based solid electrolytes and electrode materials." *Solid State Ionics,* 1989.

[20] H. J. M. Bouwmeester, C. Song, J. Zhu, J. Yi, M. Van Sint Annaland, and B. A. Boukamp, "A novel pulse isotopic exchange technique for rapid determination of the oxygen surface exchange rate of oxide ion conductors." *Physical Chemistry Chemical Physics,* 2009.

[21] C.-Y. Yoo and H. J. M. Bouwmeester, "Oxygen surface exchange kinetics of SrTi1−xFexO3−δ mixed conducting oxides." *Physical Chemistry Chemical Physics,* 2012.

[22] C.-Y. Yoo, B. A. Boukamp, and H. J. M. Bouwmeester, "Oxygen surface exchange kinetics on PrBaCo2O5+δ." *Solid State Ionics,* 2014.

[23] T. Svee, "The synthesis and transport properties of BaGd0.3La0.7Co2O6-δ." *Department of Chemistry, University of Oslo*, 2019.

[24] D. S. Tsvetkov, V. V. Sereda, and A. Y. Zuev, "Oxygen nonstoichiometry and defect structure of the double perovskite GdBaCo2O6−δ." *Solid State Ionics,* 2010.

[25] N. Ishizawa *et al.*, "Structural Evolution of GdBaCo2O5+δ (δ = 7/18) at Elevated Temperatures." *Chemistry of Materials,* 2014.

[26] C. Bernuy-Lopez, K. Høydalsvik, M.-A. Einarsrud, and T. Grande, "Effect of A-Site Cation Ordering on Chemical Stability, Oxygen Stoichiometry and Electrical Conductivity in Layered LaBaCo2O5+δ Double Perovskite." *Materials,* 2016.

[27] X. Liu, "Power Point slide," 2019.

[28] V. Thoréton, "GPA fit for MATLAB," 2021.

[29] Visual Paradigm, "Visual Paradigm Online" (2021) https://online.visual-paradigm.com/

[30] VICI "Sample Injection - Valco 6 port valve." *Valco Instruments Co. Inc.* https://www.vici.com/support/app/app11.php (accessed 13.08, 2021).

[31] V. Thoréton, "PIE fit for MATLAB," 2021.

[32] G. Wypych, "Handbook of Fillers" *4th ed. ChemTec Publishing*, 2016.

8 Appendix

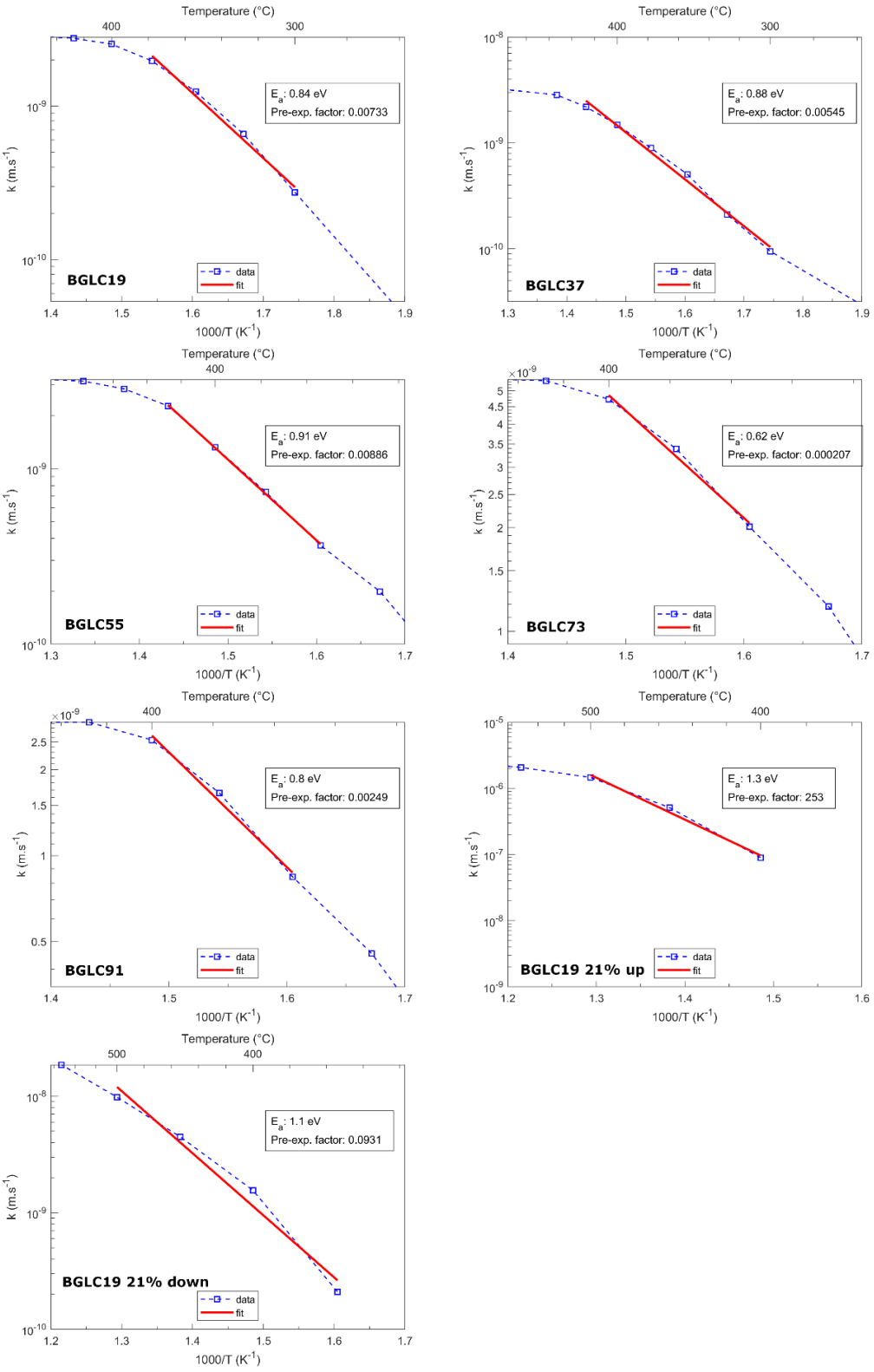

Figure 28 - Arrhenius plots for all compositions and experiments.

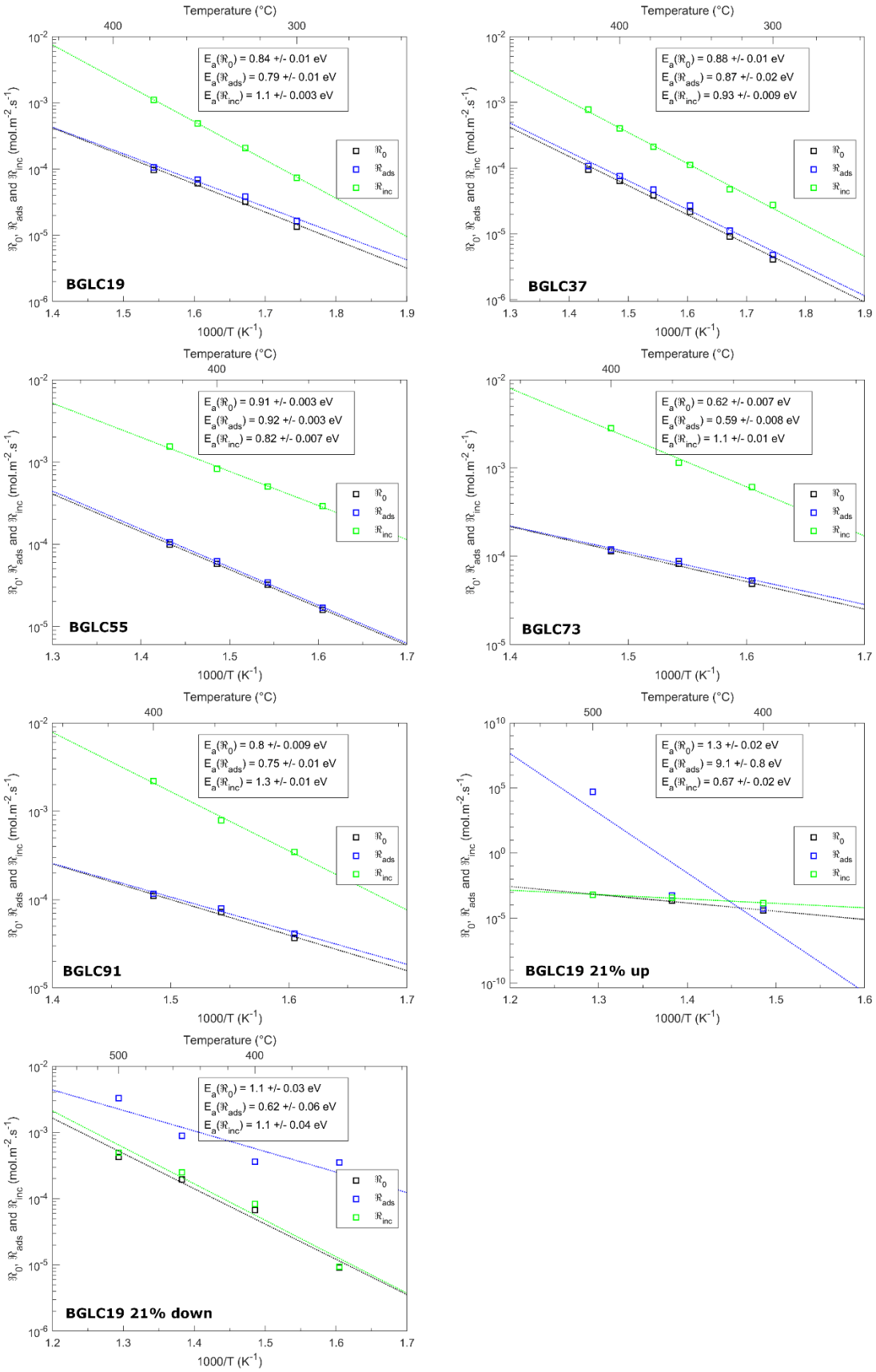

Figure 29 – Plots of calculation of reaction step energies for all compositions and experiments.

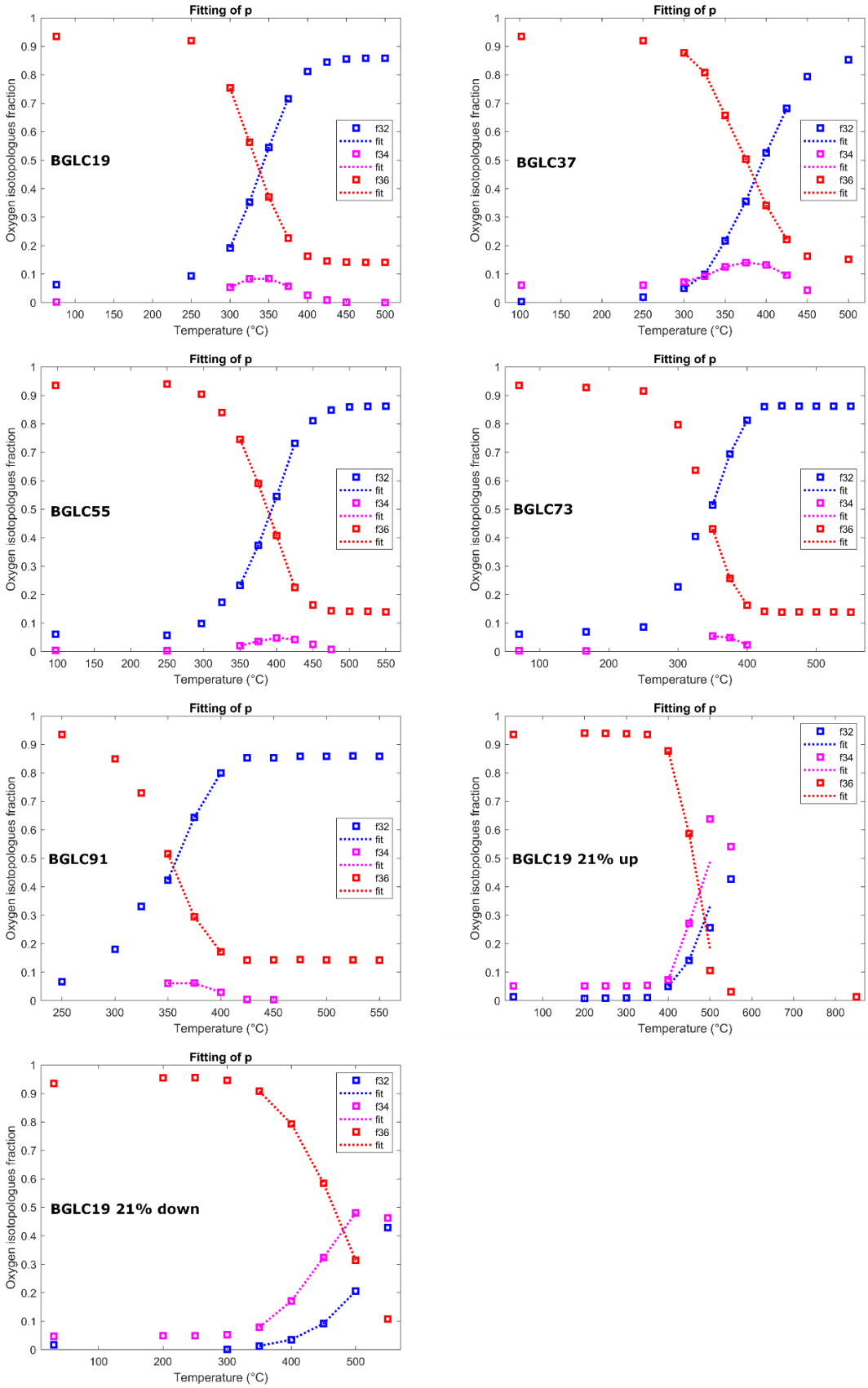

Figure 30 - Fractions of each oxygen molecule specie used for fitting of p. Data points used in calculations of reaction step energies are connected by lines.

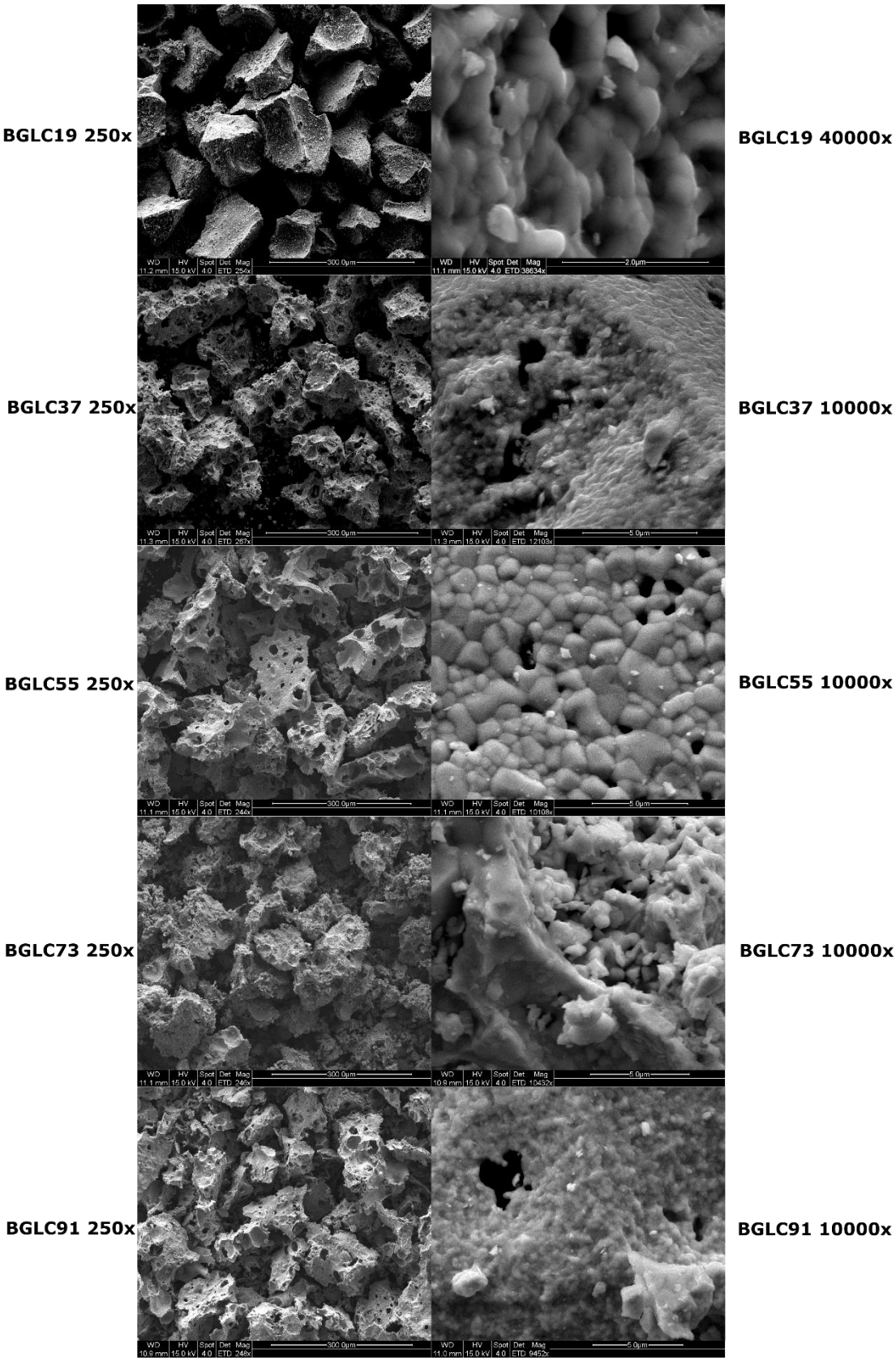

Figure 31 - SEM imagery of all synthesized BGLC compositions after sieving.